The Pennsylvania State University

The Graduate School

ADVANCED SHAPE MEMORY METAL-MATRIX COMPOSITES: RELATING NANO-FIBER REINFORCEMENT STRUCTURE TO BULK COMPOSITE SHAPE MEMORY PROPERTIES

A Thesis in

Engineering Science and Mechanics

by

Richard William LaSalle

Submitted in Partial Fulfillment
of the Requirements
for the Degree of

Master of Science

May 2021

The thesis of Richard William LaSalle was reviewed and approved by the following:

Reginald F. Hamilton
Associate Professor of Engineering Science and Mechanics
Thesis Advisor

Todd A. Palmer
Professor of Engineering Science and Mechanics

Charles E. Bakis
Distinguished Professor of Engineering Science and Mechanics

Richard F. Gordon
Medical Metals LLC

Judith A. Todd
P.B. Breneman Chair and Professor of Engineering
Science and Mechanics
Head of the Department of Engineering Science and Mechanics

ABSTRACT

NiTiNb shape memory alloys (SMAs) exhibit martensitic phase transformations (MT) at relatively higher temperatures compared to NiTi alloys as a result of the addition of Nb. Nb nano-structure fiber-like reinforcements exist within a NiTi matrix. Using thermo-mechanical experimentation and microstructural characterization of variable NiTiNb alloy wrought geometries (ring, rod, sheet, and wire), this work relates variable Nb morphologies to shape memory behavior. Utilizing deformation processing to tailor the oriented Nb morphology (i.e. discontinuous fiber size and spacing) allows for tuning the underlying MT. The ability to tune the microstructure gives the material advantageous characteristics for endoscopes for biomedical applications, civil engineering applications requiring pre-stressing, and improving resistance against fatigue Specimens were tested using differential scanning calorimetry (DSC) to determine thermal-induced martensitic transformation (TIMT) temperatures. Samples were monotonically loaded in a mechanical load frame and heated to recover using DSC. The Nb morphologies were characterized using scanning electron microscopy (SEM) to observe the resultant Nb particle size and spacing. The results show that the thermal-induced martensitic transformation is suppressed in the wrought composite structure. Post-processing heat treatment relieves the microstructure constraint so the TIMT occurs. The one-way shape memory effect (OWSME) is investigated by pre-straining the material and heating to recover under zero load, i.e. stress-free recovery. As pre-strain levels increase, the results confirm an alteration to the underlying martensitic transformation pathway that is atypical relative to the conventional response of binary NiTi.

TABLE OF CONTENTS

List of Figures

List of Tables

Acknowledgements

I would like to thank my wife, Madeline LaSalle, for supporting me through all of the good and bad times in life. She has kept me grounded and focused, motivated me to grow as a man and as a professional, and has always been there for me. Her patience and companionship has allowed me to achieve everything that I have during my time at Penn State. My mother has been another significant supporter of me throughout my whole life and has been waiting for the day that one of her sons has graduated from Penn State. She has raised me to be the man that I am today, and none of this would have been possible without her love and support throughout my life. Lastly, I would like to thank my advisor, Dr. Reginald F. Hamilton, for being an extraordinary advisor and mentor. He has allowed for me to become more of a scientist and professional than I ever thought that I could be. It was an honor to be a part of his research group and I am grateful for this wonderful opportunity that he has provided me with.

This material is based upon work supported by the National Science Foundation (NSF) under Grant No. 1538354. Any opinions, findings, and conclusions or recommendations expressed in this material are those of the author(s) and do not necessarily reflect the views of the National Science Foundation. This work was supported by the Defense Advanced Research Projects Agency (DARPA) under Agreement No. D19AP00053. Any opinions, findings, and conclusions or recommendations expressed in this material are those of the author(s) and do not necessarily reflect the views of the Defense Advanced Research Projects Agency.

Chapter 1: Introduction

1.1 Background

NiTiNb shape memory alloys were discovered in the late 1980's when it was found that the addition of Nb to NiTi resulted in a much wider hysteresis than conventional NiTi alloys (Kakeshita et al., 2000; Lanba & Hamilton, 2014; Machado & Lagoudas, 2008; Siegert, Neuking, Mertmann, & Eggeler, 2002). The NiTiNb alloys are deformed at low temperatures, typically below 0 °C, in the product martensitic phase, referred to as pre-straining. When the materials are heated to temperatures above ambient, they transform to the parent austenitic state and recover their original shape. The start temperature for the transformation to the parent phase is designated A_s and the reversion to the parent phase is complete/finished at the A_f temperature. After pre-straining martensitic NiTiNb SMAs, the A_s and A_f temperatures increase greatly compared to pre-strained conventional NiTi SMAs. Due to the large hysteresis, they could be stored and shipped near room temperature for activation via heating once in service. The shape memory response and wide hysteresis is attractive for practical applications. With increases in thermal hysteresis and mechanical behavior of the material, NiTiNb allowed for a class of SMA for use as pipe couplings and deployable biomedical devices. The compliant martensitic structure enables deployment in a heavily deformed state, i.e. pre-strained, and after activation via heating, keeps vessels open at a constant force or provides clamping/morphing functionality.

Figure 1.1 illustrates the martensitic transformation (MT) of SMAs, the crystallographic relationship between the austenitic parent phase and the martensitic phase, and the twinning and detwinning mechanisms related to superelastic and shape memory behavior. The martensitic phase transformation giving rise to shape memory behavior can be induced thermally or via stress. The MT is considered displacive since the atoms in the material do not need to move a relatively large distance (Machado & Lagoudas, 2008). Displacive transformations also indicate that there is not a change in chemical structure. The atoms can move over these short distances when thermally induced to change the structure of the material. Externally applied load changes the shape. Once the heat or stress has been

removed from material, the original parent structure and shape are recovered. The martensitic transformation is a diffusionless and first-order transformation. Twinning is the preferred deformation accommodation step with SMAs, which is reversible and thus facilitates shape recovery with increasing temperature, or unloading (Machado & Lagoudas, 2008). The shape memory effect is expected when deforming NiTiNb in the martensitic state. In the low temperature twinned structure, with many twin variants, a single variant of martensite can be stress-induced, known as detwinning. SMAs recover their original shape when raised to a higher temperature and dissipate energy via a hysteretic thermal or mechanical transition (Machado & Lagoudas, 2008). Deforming an SMA above the A_f temperature generally results in a pseudoelastic response. Martensite is stress-induced and the austenite is recovered during unloading. NiTiNb is known to exhibit a superelastic response when deformed above A_f. In the austenitic phase initially, the material will elastically deform until a critical stress is reached. The stress-induced martensitic (SIM) transformation ensues over an extended plateau region in the stress-strain response; higher stresses cause martensite to detwin and reorient (Machado & Lagoudas, 2008).

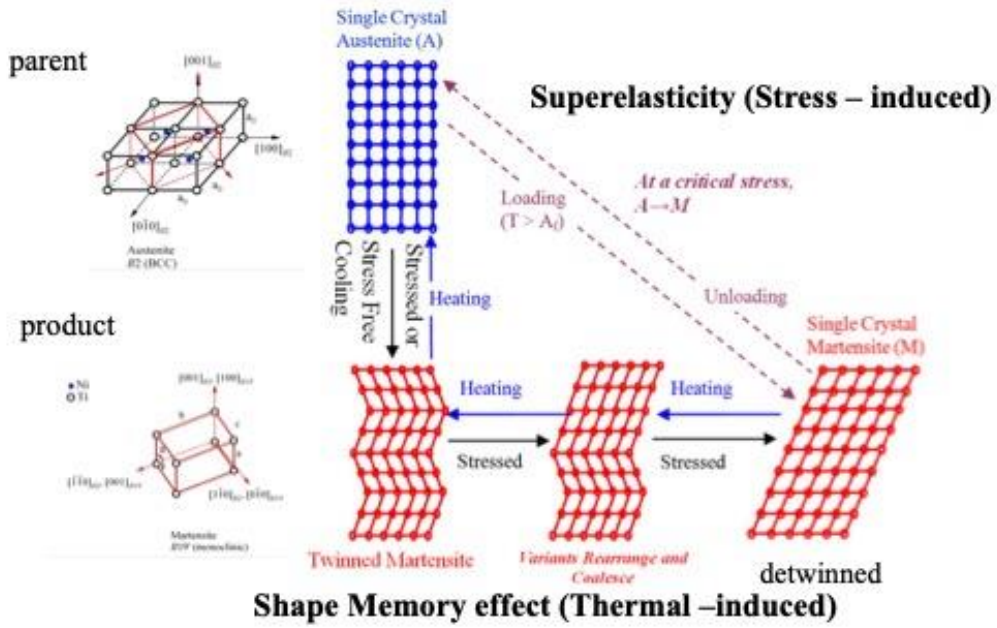

Figure 1. 1 Schematic illustration of the multi-scale martensitic transformation (MT) in shape memory alloys (SMAs). The crystallographic relationship between the austenitic B2 parent phase and martensite B19' product phase is depicted. The twinning and detwinning deformation mechanism is related to the stress-induced superelastic (SE) effect and the thermal-induced shape memory effect (SME).

1.1.1 Microstructure of NiTiNb Alloys: Influences of the Addition of Nb to NiTi, Wrought Processing and Post-processing Heat Treatment

The addition of niobium to the binary nickel-titanium SMA widens the thermal transformation hysteresis (Machado & Lagoudas, 2008), forms Nb precipitates throughout the NiTi matrix, (Piotrowski et al., 2009; Zhao et al., 1990) and enhances the energy storage. According to the work from Siegert, W; Neuking, K; Mertmann, M, the width of hysteresis changes from 40 °C to about 57-82 °C depending on the atomic percent of the Nb ranging from 5 – 21 at.% for the stoichiometric binary alloy of NiTi (Siegert et al., 2002). Beta-Nb phase is present in NiTiNb with the NiTi matrix. The study from Wei, L., & Xinqing, Z. looks at NiTiNb of 47%, 44%, and 9%, respectively, and of 49.8%, 45.2%, and 5%. (Wei & Xinqing, 2009)

Cast ingots are produced by melting Nb with NiTi. With the addition of Nb, as cast alloys exhibit eutectic microstructures, characterized by the coexistence of the austenitic B2 crystal structure, which is a high symmetry body-centered cubic austenite phase, and a bcc Nb-rich phase with a lamellar structure. The start temperature, M_s, for the forward transformation from austenite-to-martensite are dependent on the Ni/Ti ratio in the B2 Ti-Ni phase, which can contain small amounts of dissolved Nb (Piao et al, 1992; Tetsuhiko et. al. 1995). Heat treatments are used to tune the M_s temperature; the Ni/Ti ratio changes which in turn affects the M_s temperature (Y. Zheng, Cai, Wang, Luo, & Zhao, 1998). Long annealing and forging times along with hot rolling thinned out the lamellar Nb eutectic clusters into fine thin strips. The resulting crystal structures were the martensite phase, which is B19' monoclinic and has low symmetry, and the austenite phase, the B2 phase. (Duerig, Melton, & Stöckel, 1990)

1.1.2 Structure-Property Relationships: Influence of Pre-strain

He et al. found that $Ni_{50.1}Ti_{46.9}Nb_3$ (at.%) alloy has a better shape memory effect than $Ni_{47}Ti_{44}Nb_9$ (at.%) alloy. A 100% shape recovery ratio was observed up to 8% strain and the ratio remained relatively high at 55% with the onset of 24% strain. (He, Rong, Yan, & Li, 2004) He et al. concluded that the deformation of β-Nb particles and TiNi matrix phase in the $Ti_{46.9}Ni_{50.1}Nb_3$ at M_s + 30 °C can relax the elastic strain energy of martensite. This results in a widened transformation temperature hysteresis. The

$Ti_{46.9}Ni_{50.1}Nb_3$ (at.%) alloy had a much wider transformation temperature interval than the $Ni_{47}Ti_{44}Nb_9$ (at.%). (He et al., 2004)

Jiang et al. investigated martensitic transformations constrained by the microstructure (Jiang, Cui, Zheng, Zhao, & Li, 2009). The first heating exposed a wide temperature range full reverse transformation when compared to undeformed NiTiNb. Additional peaks during the heating are due to the constraining effect of the Nb on the NiTi SMA matrix. Recovery stress was induced along with the typical reverse transformation of the oriented martensite and reoriented the residual martensite that did not recover. With incomplete heating and cooling, the reoriented martensite and the stress-induced martensite were successfully induced from the austenite phase. As the temperature was cooled further, self-accommodated martensite was formed, heating of the material, three groups of martensite reverted to the austenitic phase.

Hao et al. pre-strained NiTiNb with Nb nanowires reinforcing the NiTi matrix (Hao et al., 2013). A nanostructured Nb reinforced NiTi SMA composite was fabricated by mechanical reduction of the as-cast Nb-NiTi eutectic alloy. It exhibited large elastic strain, high strength, narrow hysteresis, and high mechanical energy storage density. Coupling of nanostructured Nb and NiTi matrix during deformation is the underlying mechanism behind these properties. Wang et al. revealed that dislocations form at the interfaces between the Nb nanowires, and the NiTi matrix via pre-straining. A wide distribution of local stress amplitudes throughout the NiTiNb, a wide distribution of remnant embryonic martensitic domains, proves the MT occurs in specific locations depending on the stress field of each dislocation. (Wang et al., 2019) Zhang et al. established a relationship between the stress transfer from the SMA matrix to the Nb nanowires, volume fraction and aspect ratio of the nanowires to the matrix, and the amount of pre-strain on the material. The nanowires undergo plastic deformation. The SMA matrix behaves in the superelastic manner. The MT causes plastic deformation in the nanowire areas, and martensite remains around the nanowire in the SMA matrix. Martensitic transformations occur upon increasing loading of the material. The residual martensite around the nanowires act as nucleation sites. (Zhang et al., 2017)

He et al. prepared low niobium content, $Ni_{50.1}Ti_{46.9}Nb_3$ (at.%), and $Ni_{47}Ti_{44}Nb_9$ (at.%) which were hot swaged and rolled into rods and machined into 4 mm diameter tensile samples. The samples were

solution treated at 1113 K for 2.4 ks, and were water quenched. Transformation temperatures were obtained via electrical resistance measurement. Tensile samples were strained at 2.8 x 10^{-4} s^{-1} at a temperature of M_s + 30 °C. Following tensile deformation, reverse transformation temperatures were obtain via differential scanning calorimetry at a rate of 10 °C per minute. Scanning electron microscopy was used to obtain images of the material microstructure. (He et al., 2004)

He and Rong investigated the reverse martensitic transformation of deformed $Ni_{47}Ti_{44}Nb_9$ (at.%) (He, Rong, Yan, & Li, 2005). Specimens were processed into rod geometries with diameters of 8.5 mm and differential scanning calorimetry specimens were sectioned out of the rods. All specimens were solution treated at 860 °C for 2.4 ks and water quenched. Transformation temperatures of the heat-treated specimens were determined using differential scanning calorimetry at a rate of 0.17 °C per second. Tensile tests were conducted at a strain rate of 2.8 x 10^{-4} s^{-1} at a temperature of M_s + 30 °C. Specimens were pre-strained between the strain levels of 0% and 21% (He et al., 2005). While this study considers stress-induced and strain-induced martensite while studying NiTiNb, the US patent from Rich Gordon considered strain-induced austenite (SIA) by implementing various methods to obtain the SIA (Gordon, 2009). The work annealed a $Ni_{44}Ti_{47}Nb_9$ alloy between 650 °C and 900 °C for less than 60 minutes, cooled while under a load which strained the material to observe thermally induced TTs, the alloy was then strained between 8% and 25% to elevate A_s.

1.2 Research Problem Description

Previous works clarified the influence of deformation processing on the Nb microconstituent morphology and identified the optimal NiTiNb composition (M. Piao, Miyazaki, Otsuka, & Nishida, 1992; Siegert et al., 2002).Reports that investigate the influence of pre-strain study dependencies of the strain recovery ratios and thermal-induced recovery temperatures on pre-strain. Optimal pre-straining for widening hysteresis is recommended at temperatures below room temperature and near the M_s temperature, (M_s + 30 °C) (He & Rong, 2004). Stabilization of martensite and a wide hysteresis are attributed to the contribution of plastic deformation of Nb to strain energy relaxation (He & Rong, 2006;

Meng, Chen, Cai, Wang, & Zhao, 2006; Y. F. Zheng, Cai, Zhang, Zhao, & Ye, 2000). Optimal pre-strain temperatures and strain-levels are typical reported. More recently, the microstructure was considered as composite-like with oriented nanostructured Nb microconstituents dispersed within a NiTi matrix. Local stress/strain concentrations in the vicinity of Nb facilitate transformation to martensitic substructures during deformation (Hao et al., 2012, 2013; Jiang et al., 2009; Zhang et al., 2017). The Nb microconstituents reportedly improve mechanical properties due to stress transfer from Nb while NiTi matrix undergoes the stress-induced martensitic transformation (Zhang et al., 2017).

This experimental study investigates ring, sheet, rod and wire wrought NiTiNb alloys. Select wrought materials are pre-strained with levels increased so that accompanying high stress levels induce martensitic substructures and the thermal-induced shape memory recovery is reported. Materials are investigated in the as-received conditions and select wrought forms are investigated after post-processing heat treatment. The critical stress for inducing the transformation is decreased after heat treatment and thus this work provides an improved understanding of the influence of stress levels reached during pre-straining. Furthermore, materials were subjected to multiple thermal cycles in order to characterize the stability of thermal-induced recovery. This comprehensive study provides insights for understanding practical wrought processing for tuning the high temperature MT and wide thermal hysteresis.

1.3 Overview of Thesis

The remainder of the thesis is separated into four chapters. Chapters 2-4 include methods and results and discussion subsections. Chapter 2: Materials Characterization presents the microstructure characterization approach. SEM reveals the Nb morphologies and quantitative measurements include size and spacing. The results show the cast microstructure and the wrought alloy microstructures. In the wrought alloys, a metal matrix fiber-reinforced composite-like microstructure exist with nanostructured Nb discontinuous reinforcements oriented in the processing direction distributed within a NiTi matrix. This work reports the dependence of the reinforcement morphology on wrought processing. In Chapter 3: Thermal Analysis, the thermal-induced martensitic transformation is characterized using DSC analysis,

measuring the start, peak, and finish temperatures of endothermic/exothermic peaks. The results show that the thermal-induced MT is suppressed in the as-received condition and post-processing heat treatments can bring about thermal-induced MT, seeming to relieve a constraining effect of the nanostructured Nb fibers. Chapter 4: Pre-strain and Thermal-Induced Recovery covers the effect of pre-straining deformation. Sheet and ring wrought NiTiNb alloys are pre-strained. DSC analysis is used to characterize stress-free thermal recovery. For the sheet materials, the dependence of the unloading response on pre-strain is reported along with the stress-free thermal recovery. The results show that stress-induced martensite is stabilized after pre-straining and recovers via heating. Moreover, at pre-strain levels exceeding a critical value, an atypical stress-induced martensite occurs and thermal recovery occurs at temperatures exceeding those measured for the TIMT. The thesis concludes with Chapter 5: Summary and Recommendations for Future Work.

Chapter 2: Microstructure Characterization

2.1 Materials and Characterization Method

2.1.1 Sheet

Materials were supplied by Medical Metals LLC, Ridgefield, CT in sheet, ring, rod, and wire wrought forms. Sheet material with a composition of $Ni_{47.7}Ti_{43.5}Nb_{8.8}$ at.% was processed via cold rolling, referred to as the as-received condition. Tensile specimens with a dog-bone geometry were micromachined from the sheet using wire-EDM to the dimensions shown in Figure 2.1 in accordance with ASTM standard E8 (ASTM E8, 2010).

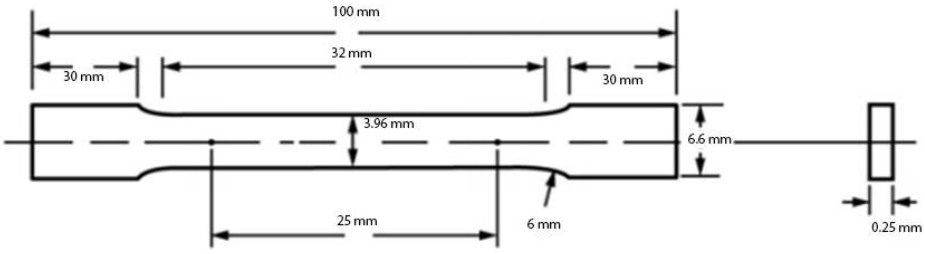

Figure 2. 1 The dog-bone shape tensile specimen design based off the ASTM standard E8. Each specimen was cut from a strip of sheet NiTiNb.

Prior to testing the $Ni_{47.7}Ti_{43.5}Nb_{8.8}$ at.% tensile specimens, sections of the material were cut and heat treated at different temperatures and times to establish the treatment that would allow for the highest M_a temperature. All heat treatments were conducted in a box furnace and water quenched immediately after being removed from the furnace. Eight samples were heat treated at temperatures of 850 °C and 900 °C for times of 10, 30, 60, and 120 minutes with and argon gas flow into the furnace. Once the proper heat treatment had been established, it was applied to the dog-bone shaped tensile specimens. Each tensile specimen was heat treated for 5, 10. 30, 60 and 120 minutes at 900 °C.

2.1.2 Ring

NiTiNb rings had a rectangular cross section with an outer dimeter of 5.4 mm, inner diameter of 4.2 mm, resulting in a width of 0.6 mm. The height was equal to 1.1 mm. Rings from Medical Metals Lot 5754 were divided into three different groups. The first group, G1, was annealed at 790 °C for five

minutes. The second group, G2, is as received from the machinist. Group 3, G3, was expanded, aged, and recovered at 166 °C. Group 4, G4, was annealed at 790 °C for one minute. Group G5, was expanded and aged to 45 °C.

2.1.3 Rod

Wrought NiTiNb rod was hot rolled and centerless ground and had a final diameter equal to 3.45 mm. Rod form Medical Metals RM001 Rev A/Material Lot A Centerless Ground was divided into two groups, S1 and S2. The S1 weighed 189 mg. The S2 weighed 126.1 mg.

2.1.4 Wire

Wrought NiTiNb wire was cold drawn to a diameter of 0.4 mm. From the Medical Metals DM-4746, groups S3, S6, and S7 are referred to as drawn off the spool. The piece used for S3 was a 7.2 mg wire, and S6 was a 43.9 mg piece of wire. The S6 and S7 groups were analyzed using different DSC methods, discussed in the section on thermal analysis. A group designated S4 is from Medical Metals DM-4747 NG. The piece used for this group was a 6.8 mg wire. An additional wire designated S5 was from Medical Metals DM-4830 (drawn off the spool) which was a 6.2 mg piece of wire that was pre-strained (value unspecified by manufacturer).

2.1.5 Scanning Electron Microscopy

Specimens examined using SEM imaging were cut using a slow-speed diamond blade saw, then were mounted in a two-part epoxy and incrementally polished using a MetPrep polisher. Each sample was polished sequentially using 600 grit, and 1200 grit sand paper. Afterwards each sample was polished using a 3 μm polishing pad with glycol poly-diamond and finished off using a 0.05 μm colloidal silica pad with powder aluminum and alcohol. Due to the finer wire diameter, polishing started with 1200 grit sand paper and followed the rest of the polishing steps just as the rings did. Once the samples were polished, they were extracted and mounted for SEM analysis. Each sample was first examined on an FEI (Philips) XL 30 Environmental Scanning Electron Microscope. For improved resolution, the samples were

examined using Thermo-Fisher (FEI) Q250 Environmental SEM. Due to the finer wire diameter, wire specimens were examined using the NanoSEM 630, which provided the highest resolution.

Select SEM images for each wrought geometry were selected to measure Nb particle spacing and sizing. Measurements were taken in the program, ImageJ, by setting a scale relative to each images known scale from the SEM and drawing lines representative of the spacing and Nb particle width.

2.2 Results and Discussion

2.2.1 Cast

Images of as-cast NiTiNb microstructure at different magnifications were taken from previous work in the Hamilton group (R. Hamilton, Lanba, Ozbulut, & Tittmann, 2015) and are shown in Figure 2.2. The microstructure of the as-cast NiTiNb exhibits a web-like eutectic structure. The lighter gray scale corresponds to the Nb. The NiTi matrix is darker.

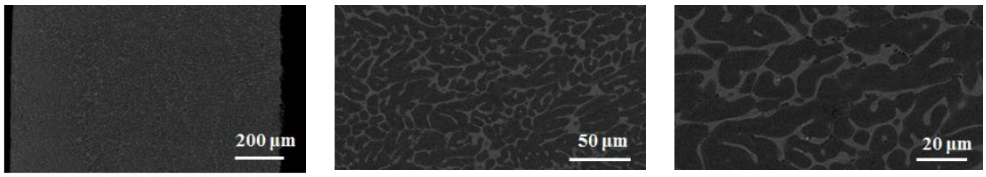

(a) (b) (c)

Figure 2. 2 Multiple magnifications of as-cast NiTiNb alloy with increasing magnification from (a)-(c).

2.2.2 Sheet

Representative images of the microstructure for each wrought sheet geometry along the processing direction are shown in Figure 2.3. All microstructure images are “as-received”. Figure 2.3(c) and 2(d) are from previous work (R. Hamilton et al., 2015; Lanba, 2015).

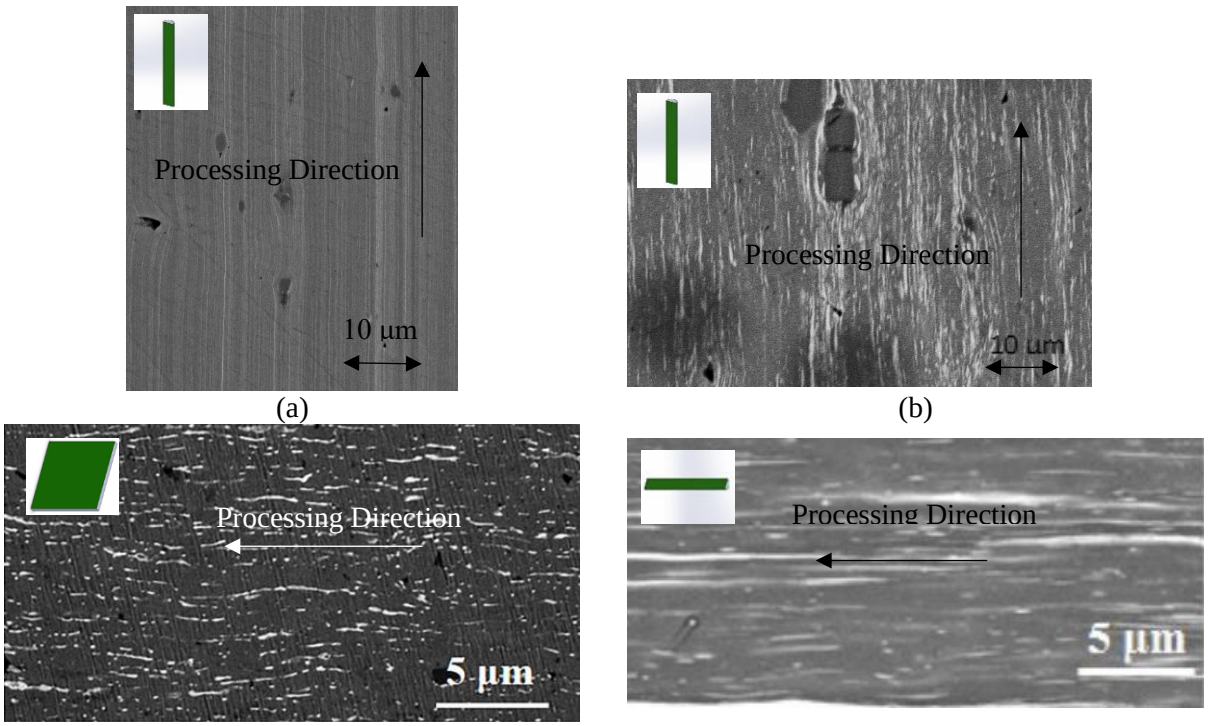

Figure 2. 3 Microstructure images from SEM showing the representative structures of each wrought geometry. (a) Shows a wire, (b) shows a ring, (c) shows a sheet, and (d) shows a rod.

2.2.3 Ring

Figure 2.4 shows images of the microstructure of the rings. Each image appears to show similar Nb particle orientation and size and spacing with respect to the processing direction. Figures 2.4(d)-(f) show the cross-section area that is perpendicular to the processing direction. Figure 2.5 shows additional microstructure images for the G3 ring along the processing direction taken on the Thermo-Fisher (FEI) Q250 Environmental SEM.

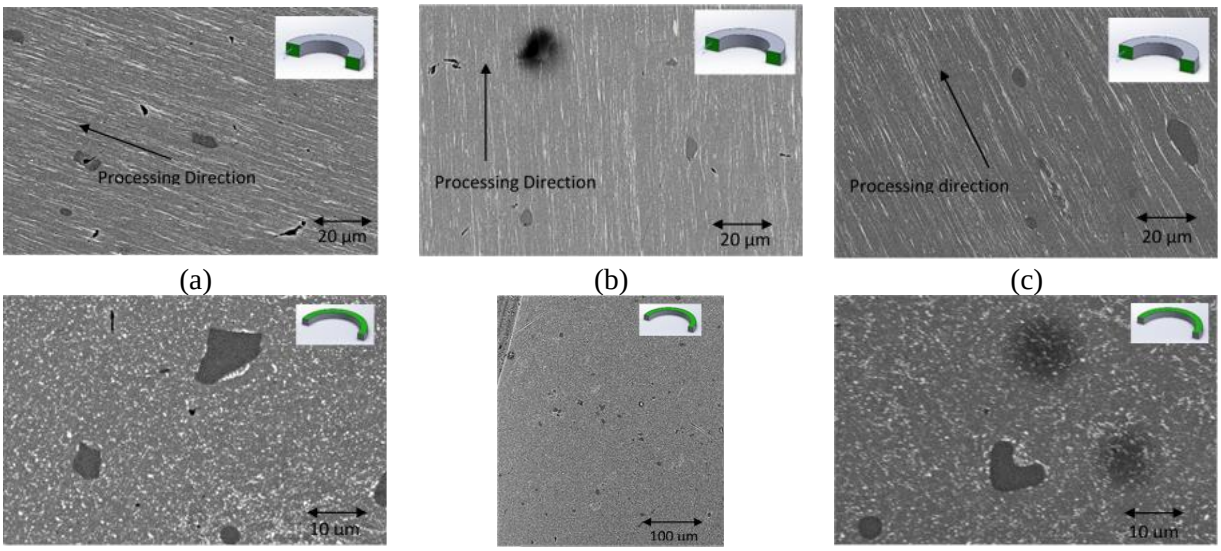

(a) (b) (c)

(d) (e) (f)

Figure 2. 4 SEM images for (a) G3, (b) G5, and (c) G2 along the longitudinal direction, and (d) G3, G5, and G1 over the latitudinal cross sectional area.

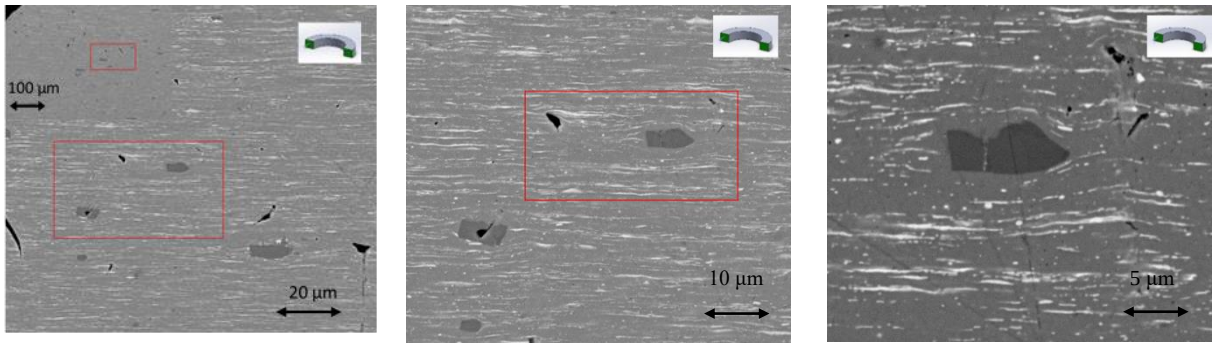

(a) (b) (c)

Figure 2. 5 SEM images of the G3 specimen taken by the Thermo-Fisher (FEI) Q250 Environmental SEM. (a) shows the cross-sectional area of the ring at a low magnification and a zoomed in view of the red boxed region, (b), and (c) show images with increasing magnification as the focus is on a Ni-rich NiTi feature in the material. Surrounding the feature are the bright Nb fiber reinforcements that are distributed throughout the NiTi matrix. The Nb fiber reinforcements are in the processing direction of the material.

2.2.4 Wire

Figures 2.6 shows various images of NiTiNb wire S3 along the processing direction, showing the much thinner Nb particle size relative to the ring geometry Nb particles. A notable difference between the as-received ring and wire microstructure is Nb fibers embedded in the wire geometry are much thinner.

However, the Nb fibers in the wire specimen appear to be relatively longer, or more continuous. Each ring exhibits similar Nb morphology orientation and particle size and shape, discontinuous fiber reinforcements oriented in the processing direction at which the ring was extruded in.

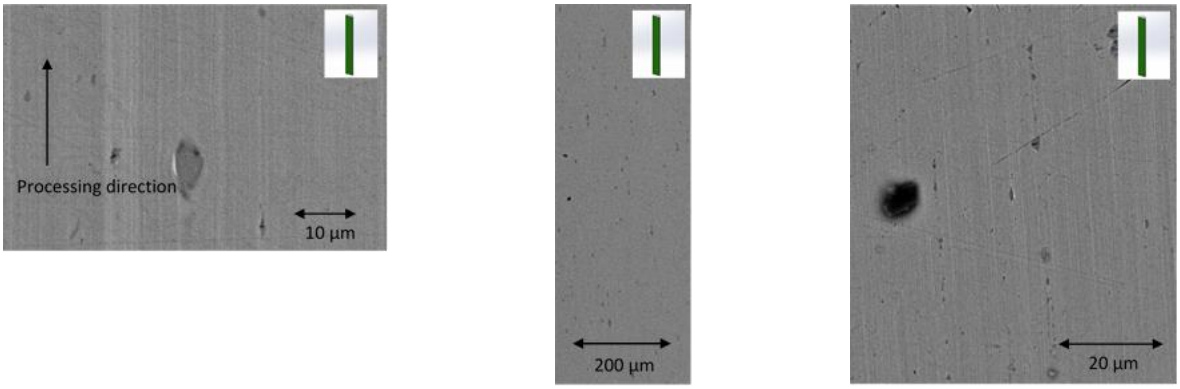

(a) (b) (c)

Figure 2. 6 SEM images for (a) S3, (b) S3 at a low magnification on the FEI NanoSEM 630, and (c) S3 at a higher magnification on the FEI NanoSEM 630 along the longitudinal direction.

The images in Figure 2.7 show the microstructure for the S4 and S5 NiTiNb wire. Recall the wires had not been heat treated, but S5 was pre-strained. Figures 2.7 (b)-(d) show the S5 wire taken from two different SEM instruments at various magnifications in order to scrutinize the Nb in the processing direction. Figure 2.8 displays images of the same specimen again, on the FEI NanoSEM 630 with various magnifications, and specifically 2.8(c) includes two measurements of Nb fiber width at 26.9 nm and 43 nm.

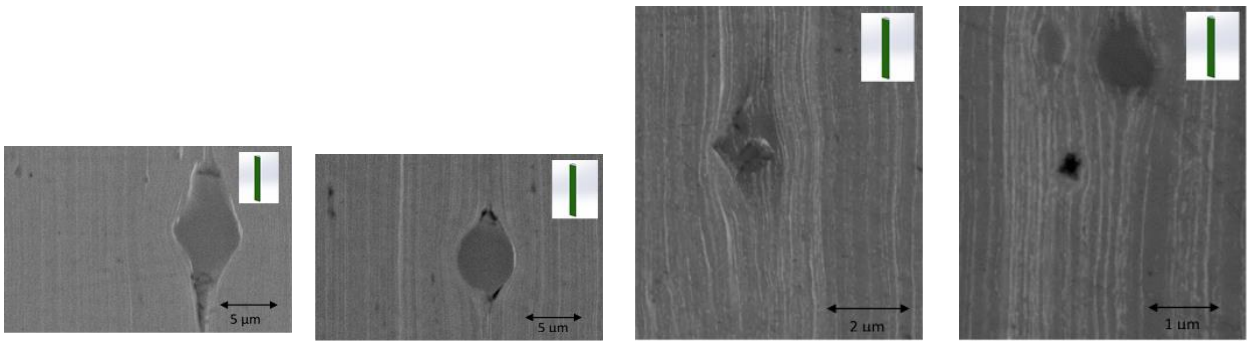

(a) (b) (c) (d)

Figure 2. 7 SEM images for (a) S4, (b) S5, along the longitudinal direction. (c) and (d) are SEM images of S5 along the longitudinal direction, taken on the FEI NanoSEM 630 at higher magnifications.

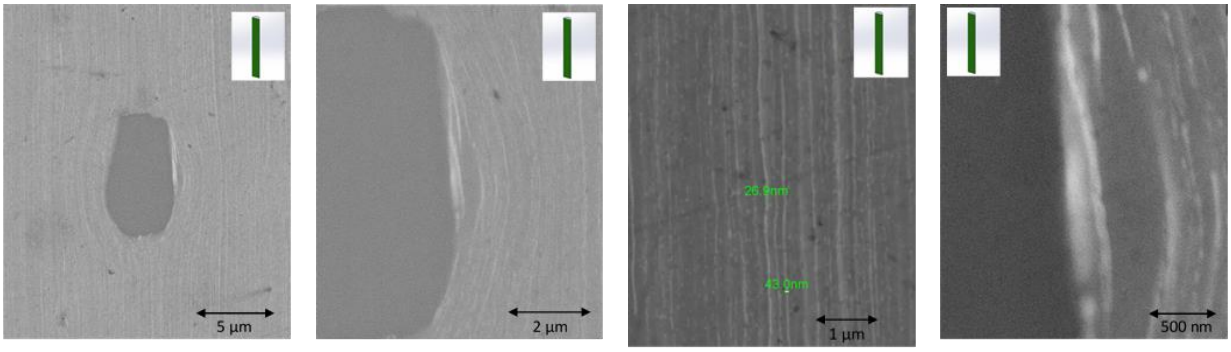

(a) (b) (c) (d)

Figure 2. 8 SEM images of the S5 wire taken from the FEI NanoSEM 630 at increasing magnifications (a)-(d).

2.2.5 Nb Morphology: Quantitative Analysis

To quantitatively study the microstructure of each NiTiNb geometry, the SEM images were analyzed using a digital measurement method in the software, ImageJ. Table 2.1 lists the geometry, initial material condition, specimen ID, and average Nb particle size by the measurement of width, and the average Nb particle spacing. The width of each Nb particle is defined by the measurement perpendicular to the processing direction of the alloy. Recall the sheet material had a composition of $Ni_{47.7}Ti_{43.5}Nb_{8.8}$ at.%, the rod had a composition of $Ni_{44.6}Ti_{42.8}Nb_{12.6}$ at.%, the wire was $Ni_{48.8}Ti_{37.18}Nb_{14.02}$ at.%, and the ring possessed a proprietary composition within the range of the sheet and wire. The ring exhibits the largest Nb particle widths and spacing and they become smaller for the sheet, rod. The wire exhibits exceptionally small Nb width and spacing. The measurements for the rod are closest to the wire.

Table 2. 1 The average Nb particle width and spacing measurements for each wrought geometry analyzed using SEM with some variation processing and post-processing treatment.

Geometry	***Initial Material Condition***	***Specimen ID***	***Average Nb Particle Size (Width nm)***	***Average Nb Particle Spacing (nm)***
Sheet	As-received		125	145
Sheet	Annealed 900 °C for 1 hr.		259	484
Rod	As-received		110	178
Wire	As-received	S3	35	48.8
Wire	As-received	S4	33.8	62.8
Wire	As-received/pre-strained	S5	36.4	74
Ring	Annealed at 790 °C for 5 minutes	G1	265	646
Ring	As-received	G2	358	489
Ring	Expanded, aged, and recovered at 166 °C	G3	406	405
Ring	Expanded, aged to 45 °C	G5	225	583

Chapter 3: Thermal Analysis

3.1 Methods: Differential Scanning Calorimetry

For the first five groups, G1 through G5, a method referred to as Method 1 was used for the DSC. Method 1 starts at 25 °C, cools from 25 °C to -120 °C at 20 °C/minute (cooling segment 1), holds at -120 °C for 3 minutes, heats from -120 °C to 150 °C at 20 °C/minute (heating segment 1), holds at 125 °C for 3 minutes, cools from 150 °C to -120 °C at 20 °C/minute (cooling segment 2), holds at -120 °C for 3 minutes, heats from -120 °C to 150 °C at 20 °C/minute (heating segment 2), holds at 150 °C for 3 minutes, cools from 150 °C to 25 °C at 20 °C/minute (cooling segment 3), and ends at 25 °C. A second method was used for groups S1-S5. Method 2 follows the same structure as method 1, but the maximum temperature is 125 °C, rather than 150 °C. The last group of S6 and S7 are the same sample, but was put through two different methods for the DSC. This Method 3 is the same as method two, but there is an additional heating segment at the end following a cooling segment to -120 °C. The $Ni_{47.7}Ti_{43.5}Nb_{8.8}$ at.% tensile samples were tested using the following procedure; (1) starting at 25 °C, (2) cooling to -120 °C, (3) holding for 1 minute, (4) heating to 150 °C, (5) holding for 1 minute, (6) cooling to -120 °C, (7) holding for 1 minute, (8) heating to 150 °C, (9) holding for 1 minute, (10) cooling to -120 °C, (11) holding for 1 minute, and (12) heating to 25 °C. A rate was 10 °C /min in accordance with the ASTM Standard F2000-17 (ASTM International, 2004). Faster scan rates of at 20 and 40 °C /min were employed in some cases.

3.2 Results and Discussion: As-received Wrought Alloys

3.2.1 Ring

Figure 3.1 shows the DSC analysis results for the material in ring form. This sample is as-received. Peaks corresponding to the forward austenite-to-martensite transformation arise around the

same temperature on each cooling curve. In the two heating segments, peaks corresponding to the reverse martensite-to-austenite transformation is observed around the same temperature.

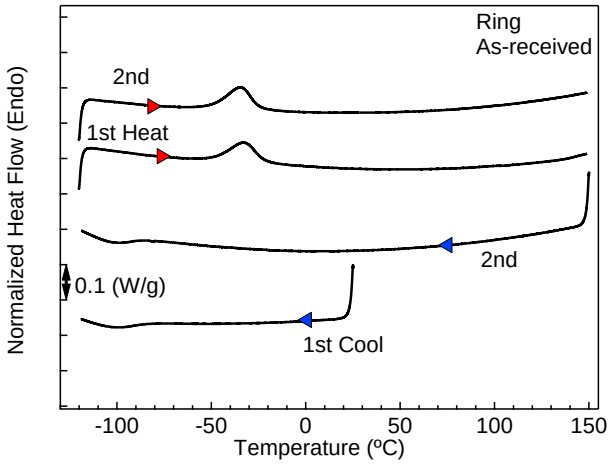

Figure 3. 1 DSC heat flow vs temperature thermo-grams for a NiTiNb alloy in ring form for group G2.

3.2.2 Wire

Figures 3.2 and 3.3 show the DSC analysis results for the wire, $Ni_{47.7}Ti_{43.5}Nb_{8.8}$ at. %. Each sample of NiTiNb went through two cycles. No thermal transitions occurred during the DSC temperature scans.

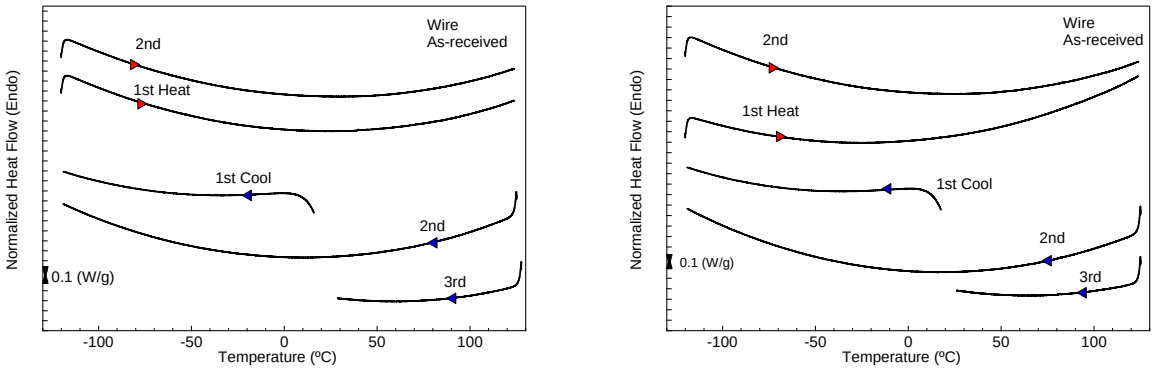

Figure 3. 2 DSC heat flow vs temperature thermo-grams for NiTiNb alloys in wire form for (a) SW3, which was off the spool with a mass of 7.2 mg and (b) SW4, which is also drawn off the spool.

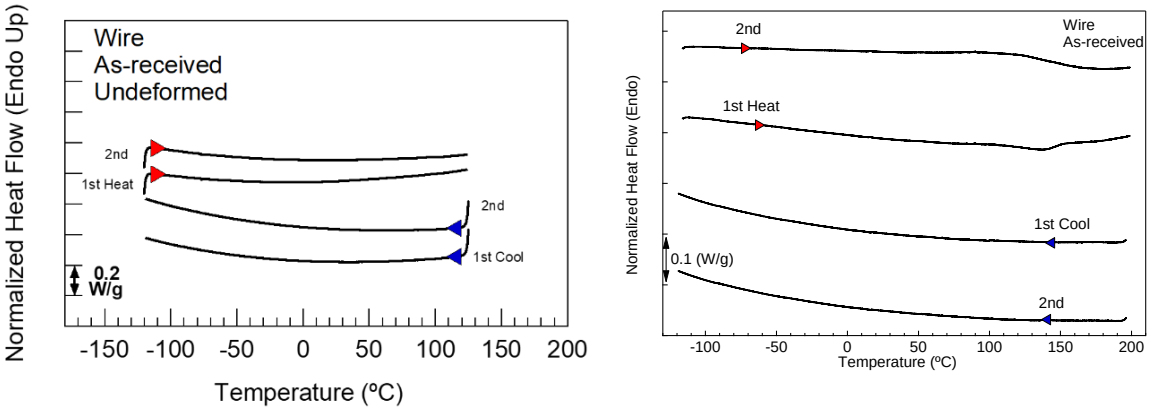

(a) (b)

Figure 3. 3 DSC heat flow vs temperature thermo-grams for NiTiNb alloys in wire form for (a) S6, which was off the spool with a mass of 43.9 mg and (b) S7, which was the same as S6, except the sample was put through a wider temperature scan.

3.2.3 Rod

Figure 3.4 shows the DSC analysis results for the rod. For each of the heating segments, there are two similar peaks at the same temperature. In the two cooling segments, peaks appear around the same temperature, albeit the transformation temperatures were difficult to measure.

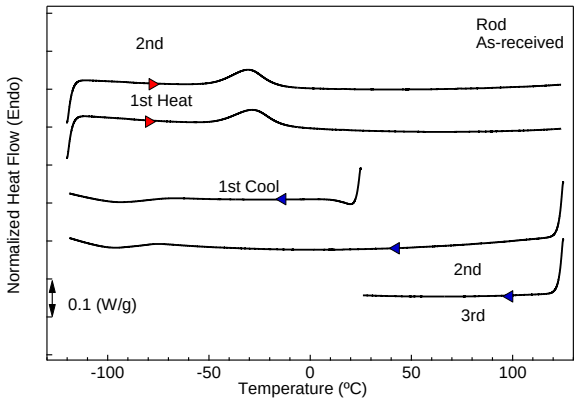

Figure 3. 4 DSC heat flow vs temperature thermo-gram for NiTiNb alloys in rod form.

3.2.4 Sheet

Figure 3.5 shows the DSC thermo-gram of an as-received sheet specimen under these conditions. Without any heat treatment or deformation, no peaks indicating any phase transitions were detected and recorded by the calorimeter. Apparently, the as-received material does not undergo the thermal-induced transformation is suppressed, likely due to residual internal stresses formed during processing.

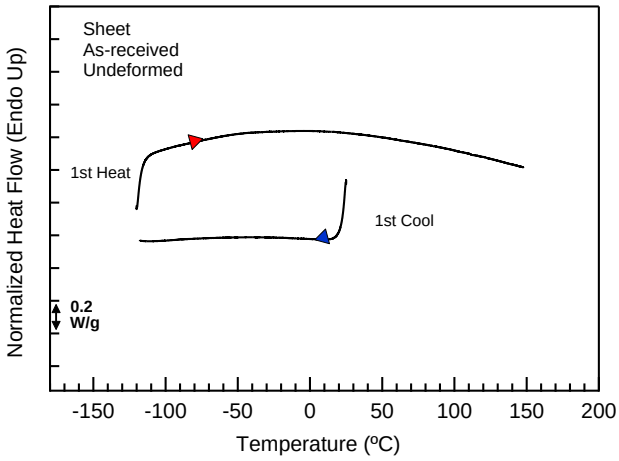

Figure 3. 5 DSC heat flow vs temperature thermo-grams for NiTiNb alloy as-received in sheet form.

3.3 Results and Discussion: Heat Treated Wrought Alloys

3.3.1 Ring

Figure 3.6 shows the DSC analysis results for the ring. The results for the sample in Figure 3.6(a) correspond to material G4 that was annealed for 1 minute at 790 °C and was thermal cycled according to the segments for method M1. There are two similar peaks at the same temperature on both heating cycles. There are also two similar peaks around the same temperature on the two cooling segments. The Figure 3.6(b) is the DSC analysis result for the group G1 material, which was annealed at 790 °C for five minutes. Two similar peaks arise at the same temperature for both heating segments and, likewise for the two cooling segments.

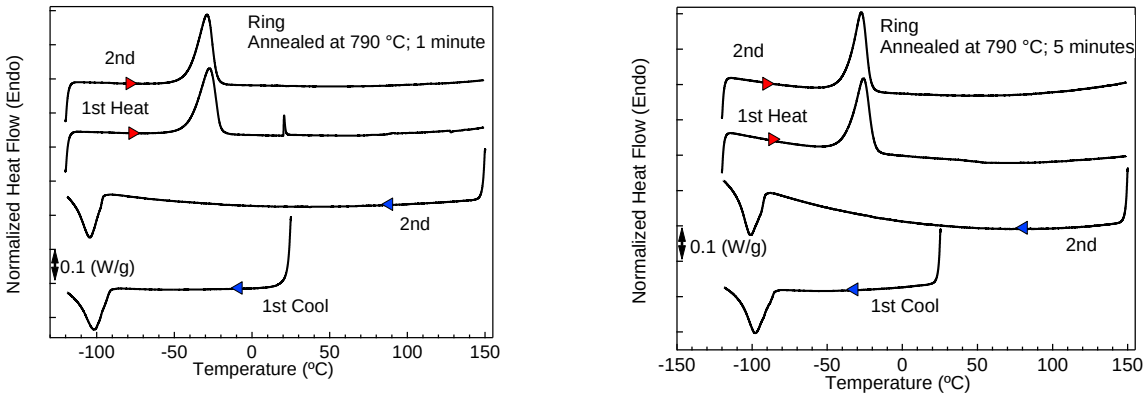

(a) (b)

Figure 3. 6 DSC heat flow vs temperature thermo-grams for NiTiNb alloys in ring form for (a) G4, which was annealed at 790 °C for one minute and (b) G1, which was annealed at 790 °C for 5 minutes.

3.3.2 Sheet

Figure 3.7 shows the thermal response of NiTiNb sheet material that had been subjected to various heat treatment times at 900 °C. Figure 3.7(a), (b), and (c) show the thermal response for annealing times of 5, 10 and 120 minutes, respectively. Annealing for 5 minutes and 10 minutes provided similar calorimetric responses. The results for the 120 minute duration show a reduced height of the transformation peaks, which in turn, reduced the enthalpy (represented by the peak area) produced during each transition.

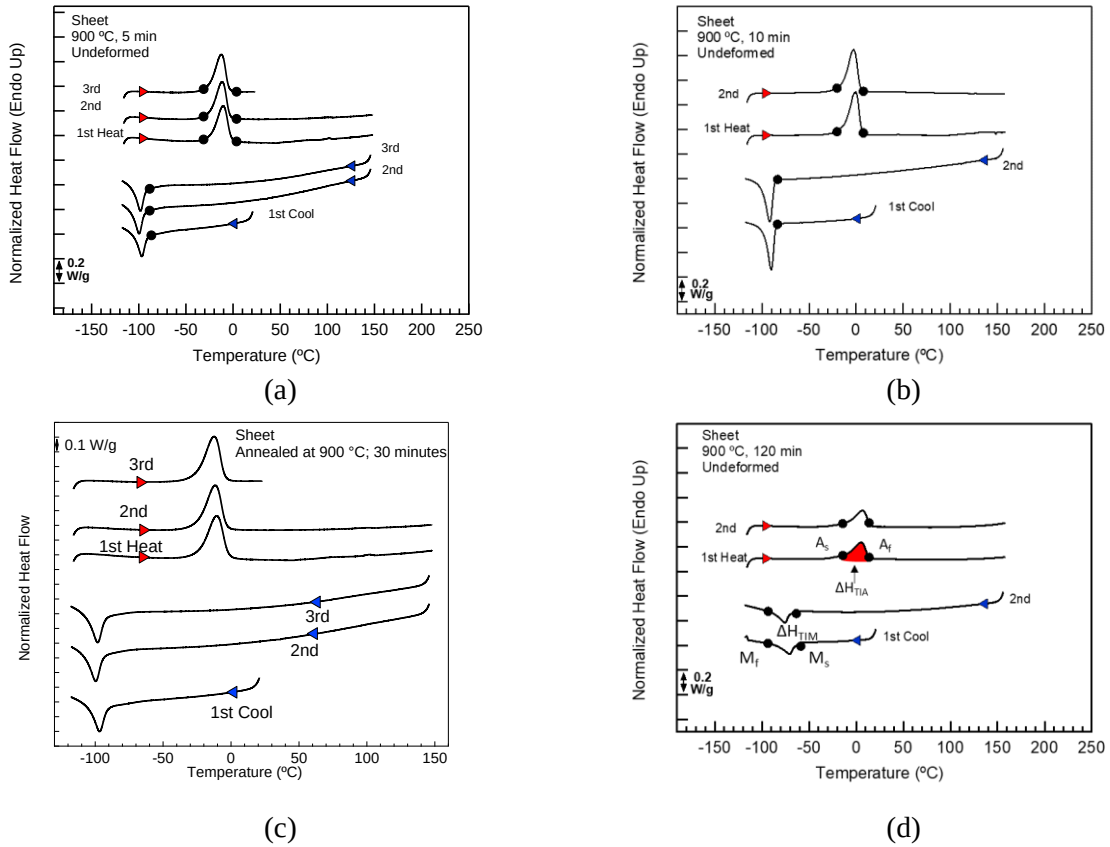

Figure 3. 7 DSC heat flow vs temperature thermo-grams for NiTiNb alloys that have been annealed at 900 °C for (a) 5 minutes, (b) 10 minutes, (c) 30 minutes and (d) 120 minutes. (c) Indicates the start and finish temperatures for the martensitic and austenitic transformations as well as the change in enthalpy as indicated by the red shading on the first heating segment.

.

Chapter 4: Pre-strain and Thermal-Induced Recovery

4.1 Ring and Wire

4.1.1 Methods

The ring and wire geometry NiTiNb material explored in this work were pre-strained using a method proprietary to the supplier, Medical Metals LLC. The recovery via heating was conducted via DSC as mentioned in the thermal analysis chapter. The supplier provided as-received rings with four pre-strain values: 14.4%, 16.5%, 18.8%, and 21.1% and the group is referred to as 64F. These rings all followed the same DSC test procedure of (1) starting at 25 °C, (2) cooling to -120 °C, (3) holding for 3 minutes, (4) heating to 125 °C, (5) holding for 3 minutes, (6) cooling to -120 °C, (7) holding for 3 minutes, (8) heating to 125 °C, (9) holding for 3 minutes, (10) cooling to -120 °C, (11) holding for 3 minutes, and (12) heating to 25 °C. The rate of each temperature scan was 20 °C/min. The DSC analysis methods for the remaining groups in the Results and Discussion section were outlined in the Thermal Analysis section.

4.1.2 Results and Discussion

Figure 4.1 shows the DSC analysis results for the ring. The results for the sample in Figure 4.1(a) correspond to material G3. This sample was expanded, aged, and recovered at 166 °C. It went through two cycles of DSC. In this plot there were not any definite peaks on either of the heating segment or on the cooling segments. The results in Figure 4.1(b) correspond to the material G5. This sample was expanded and aged to 45 °C. It went through two cycles of DSC as well. The martensite-to-austenite forward transformation peak is observed during the first heating segment only.

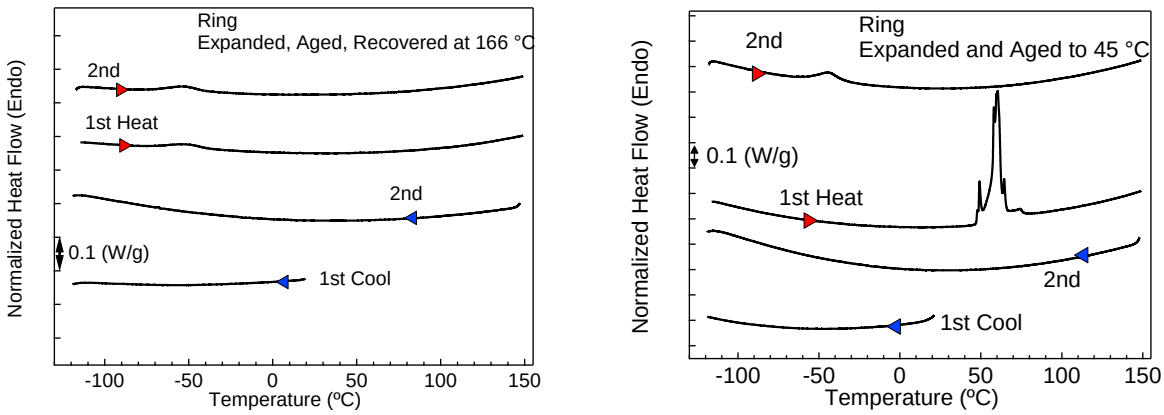

Figure 4. 1 DSC heat flow vs temperature thermo-grams for NiTiNb alloys in ring form for (a) G3, which was expanded, aged, and recovered at 166 °C and (b) G5, which was expanded and aged to 45° C.

The DSC results for the 64F group of rings are shown in Figures 4.2 and 4.3. Figure 4.2(a) and 4.3(a) shows the DSC results for the tests done on the 64FA rings that had been expanded to 14.4% strain. Figure 4.2(b) and 4.3(b) shows the DSC results for the tests done on the 64FB rings that had been expanded to 16.5% strain. Figure 4.2(c) and 4.3(c) shows the DSC results for the tests done on the 64FC rings that had been expanded to 18.8% strain. Figure 4.2(d) and 4.3(d) shows the DSC results for the tests done on the 64FD rings that had been expanded to 21.1% strain. The Figures 4.4(a) and 4.4(b) show the transformation temperature for each pre-strain. In the figures, the transformation temperatures increase when strained to higher percentages. Most importantly, the increase in A_f from the first cycle shows the most significant differences with the largest increases with the pre-strains of 18.8% and 21.1%.

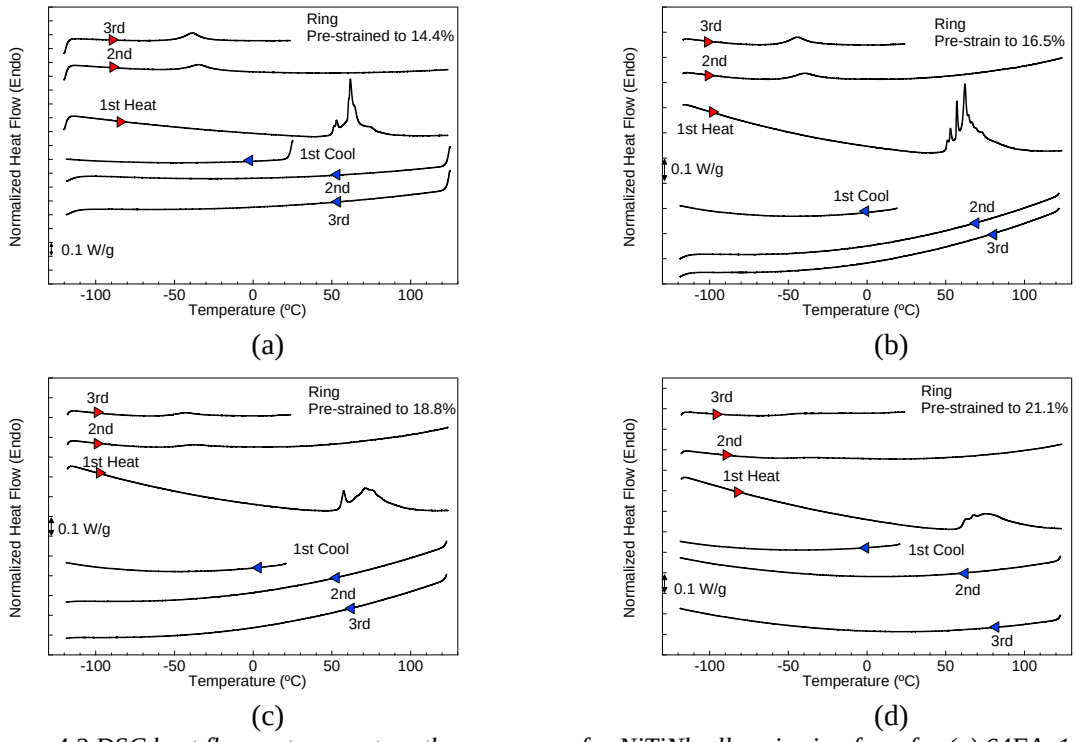

Figure 4.2 DSC heat flow vs temperature thermo-grams for NiTiNb alloys in ring form for (a) 64FA_1, (b) 64FB_1, (c) 64FC_1, and (d) 64FD_1 ranging from pre-strain values of 14.4% to 21.1%.

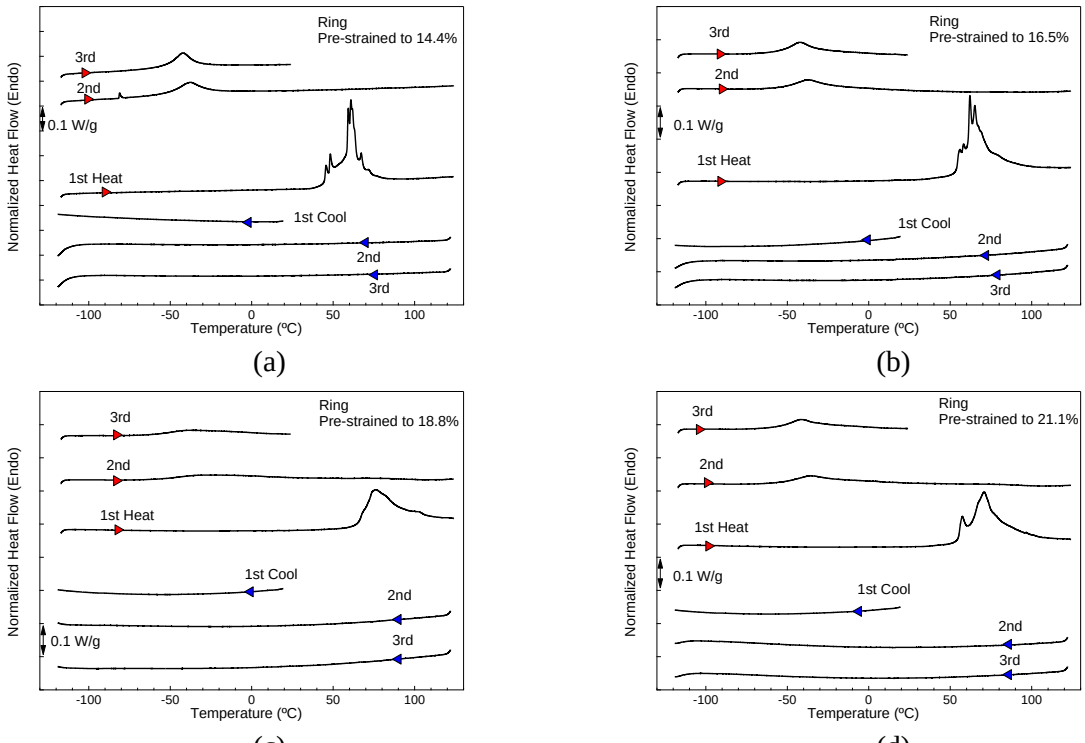

Figure 4. 3 A second set of DSC thermo-grams for the 64F rings that were pre-strained to (a) 14.4%, (b) 16.5%, (c) 18.8%, and (d) 21.1%.

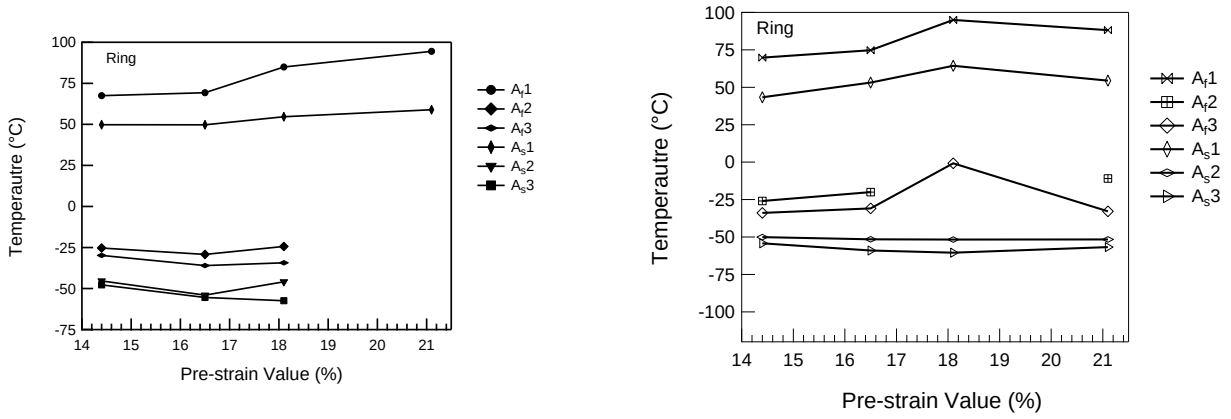

Figure 4. 4 (a) The varying transformation temperatures for each ring in batch 1 and (b) 2 as they relate to the extent of deformation. There are three sets of temperatures for each specimen due to the three cycles that the rings were subjected to during the calorimetry experiments

Figure 4.5 shows the DSC analysis of the wire material S5. A single peak arises during the reverse martensite to austenite transformation upon the first heating only. This one-time peak is likely a result of the pre-strain on the wire. The peak area is narrowest compared to the ring and the sheet, which is considered in the following section.

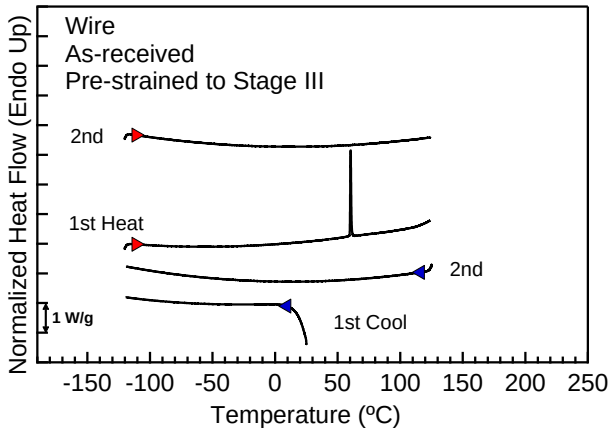

Figure 4.5 DSC heat flow vs temperature thermo-grams for NiTiNb alloys in wire form for S5, which was pre-strained drawn wire with a mass of 6.2 mg. A single high-temperature peak is observed upon the first heating segment of the wire and is not repeated during subsequent heating of the alloy.

4.2 Sheet

4.2.1 Methods: Mechanical Deformation and Localized Deformation Measurement using Digital Image Correlation

Detailed background on DIC is provided elsewhere (R. F. Hamilton, Bimber, Taheri Andani, & Elahinia, 2017; Lanba, 2015; Lanba & Hamilton, 2015; Last, 2019).$Ni_{47.7}Ti_{43.5}Nb_{8.8}$ at.% tensile specimens were prepared by applying, a speckle pattern to the gage section of the specimen using an IWATA Micron-CMB airbrush. The specimens were coated in white paint with a black paint lightly sprayed afterward, which produced a high contrast speckle pattern on the specimen surface.

The specimen was loaded and deformed using a servo-hydraulic MTS load frame with a 25 kN load cell. Experiments were carried out at room temperature. The test program implemented (1) loaded, (2) unloaded, and (3) held close to zero prior to removing the specimen for extracting DSC samples. The specimens were initially loaded to 10 N. For DIC, a machine-vision system was set up which included a Grasshopper GRAS-20S4M/C CCD camera, with a pixel array of 1600 x 1200 pixels. Fiber optic gooseneck lights illuminated the surface. The machine vision set-up can be seen in Figure 4.6, as well as the finished product of the speckle patterns.

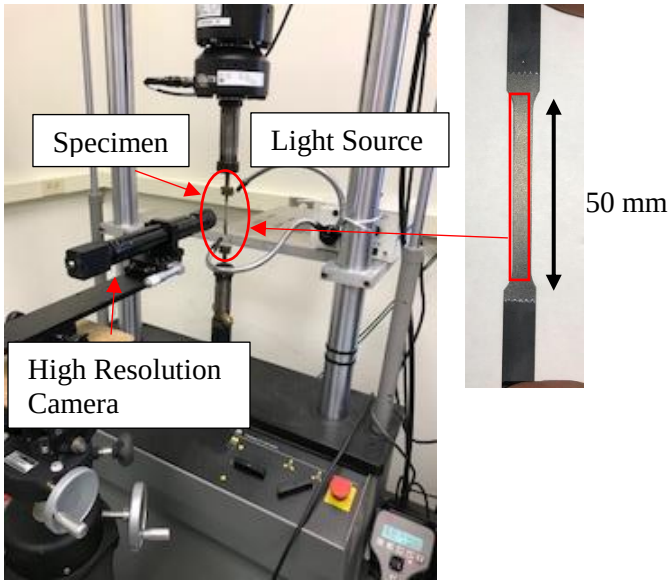

Figure 4. 6 The machine vision set-up of the camera used for DIC and the MTS load frame used to apply the mechanical load to the NiTiNb specimen and the final result of the speckle pattern on the NiTiNb tensile bar gage section.

The specimen was loaded in displacement control at a rate of 0.005 mm/sec in accordance with ASTM standard E8. The specimen was unloaded in force control at a rate of 2 N/sec. Limit detectors for both displacement during the loading segment and force during the unloading segment were implemented to reduce the risk of damaging the machine or the specimens. Each test was set to load up to 10% strain, which is 2.5 mm since the gage length of each specimen was 25 mm. The unloading segment ended at 10 N so that a small tension force was still applied to the specimen at the end of the experiments.

The Vic-Snap program was also set to take an image of the surface of the specimen every second during the mechanical test. The Vic-Snap system synchronizes image capture with force, displacement, and time data during the experiments. Each image was cropped to focus on the area of interest (AOI) and imported into the Vic-2D Correlated Solutions software for DIC measurement analysis. The AOI selected covered in the speckle pattern along the gage length and the subset size was 27 and the step size was 7. From the analysis a series of strain contours were created for the axial, transverse, and shear components of the strains.

$Ni_{47.7}Ti_{43.5}Nb_{8.8}$ at.% tension specimens were machined to the dimensions shown in Figure 2.1. As-received sheet material was deformed until failure. The same process was followed for heat treated specimens. One specimen was heat treated for 30 minutes at 900 °C and deformed to failure. The heat treatment used for the bulk of experimentation was 900 °C for 5 minutes. Additional as-received and heat treated specimens were pre-strained to 10%, 13%, 15%, 17%, 20%, 25%, 30%, and 33% and unloaded.

4.2.2 Results and Discussion

4.2.2.1 Pre-strain

Figure 4.7(a) shows the stress-strain response resulting from the stress-induced martensitic transformation for an as-received sheet deformed into the first stage of deformation out of three illustrated in 4.7(b). Markers are placed along the loading path to identify where DIC images are analyzed. In Figure 4.7(a) the stress-strain response is the elastic deformation of the austenite, a linear to non-linear response, and the stress plateau until the martensitic transformation is complete. Figures 4.8, 4.9 and 4.10

show the representative DIC contour images of the axial, transverse, and shear strain contour, respectively, for loading and unloading. For the axial strains, macro-scale engineering strains in the stress-strain curves differ from the meso-scale, local values and the true strain values determined using DIC. The macro-scale engineering strains were calculated using the actuator displacement while DIC measurements focus on the gage section in the AOI. The engineering axial strains reached 10% and maximum local axial strains reached 9%. Figure 4.7 shows the nucleation site for the martensitic transformation in image 4. The following images show the growth of the martensite as strain increases until the AOI is completely martensitic, indicated by the red shading. Images 10-13 show diffuse surface strain contours upon unloading of the specimen. Figure 4.8 shows the corresponding transverse surface strain contours with the scale bar indicating Poisson effects as the values become more negative as the axial strain increases. Image 4 in Figure 4.8 shows a similar nucleation site for the martensitic transformation and growth as strain increases in the following images. Figure 4.9 shows the corresponding surface shear strain contours reading values between 0.8% and -0.4%. This figure shows a similar nucleation site for the martensitic transformation, but minimal evidence of martensite growth.

Figure 4.7(b) shows stress-strain responses until failure for as-received and heat treated materials. Beyond the plateau region, the martensite undergoes elastic deformation followed by a linear to non-linear transition into a final strain-hardening plastic deformation until failure. Figure 4.10 shows the representative DIC contour images of the axial strain corresponding to the as-received stress-strain response in Figure 4.7(b). From the plot in 4.7(a), the elastic modulus during loading was 27 GPa, the yield stress based off the deviation from linearity was 560 MPa, the yield stress based off a 0.2% offset was 540.80 MPa, and the elastic modulus of the unloading segment is 18 GPa. The martensite elastic modulus of the as-received specimen in Figure 4.7(b) was 23 GPa with a yield stress of about 560 MPa. The heat-treated specimen has a martensite elastic modulus of 6.7 GPa and a yield stress of about 140 MPa. The elastic modulus of the austenite for the as-received specimen was 2.8 GPa, and 0.8 GPa for the austenite in the heat-treated specimen. The strain at failure for the as-received specimen was about 36%, and about 46% for the heat-treated specimen. The heat-treated specimen exhibits 10% more strain before

failure, has an elastic modulus of martensite about one-third, and a yield stress that is one-fourth of that of the as-received specimen.

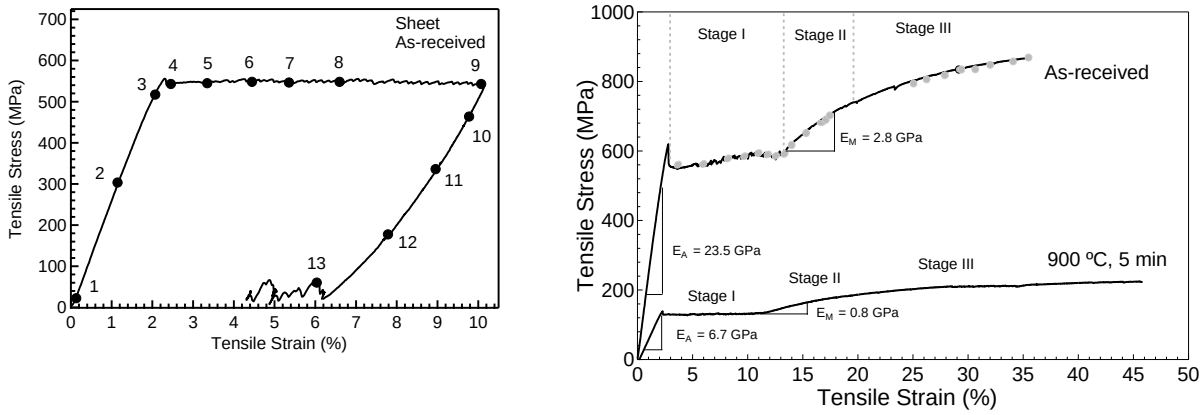

(a) (b)

Figure 4.7(a) The engineering stress versus engineering strain of a tensile $Ni_{47.7}Ti_{43.5}Nb_{8.8}$ as-received specimen pulled to 10% . (b) The deformation to failure of an as-received $Ni_{47.7}Ti_{43.5}Nb_{8.8}$ tensile specimen and a heat treated $Ni_{47.7}Ti_{43.5}Nb_{8.8}$ tensile specimen. The first stage of martensite forms between 2.8% and 13.2% strain. The second stage of martensite forms between 13.2% and 16.8% strain. The third stage of martensite forms between 16.8% and 30.6% strain and the specimen failed at about 36% strain. The markers indicate the strain value that each DIC is related to.

+

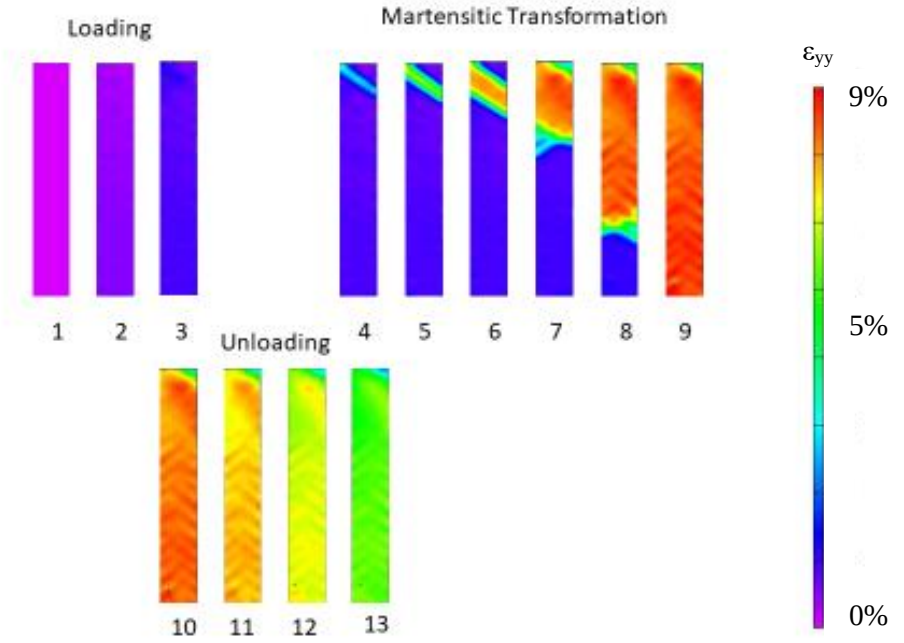

Figure 4.8 The axial strain contours of the sheet specimen during loading until maximum strain of 10% had been achieved in Figure 4.7(a). The figure includes the elastic loading contours, the loading during the martensitic transformation contours, and the unloading contours. A scale is provided to provide a numerical association with the contour colors.

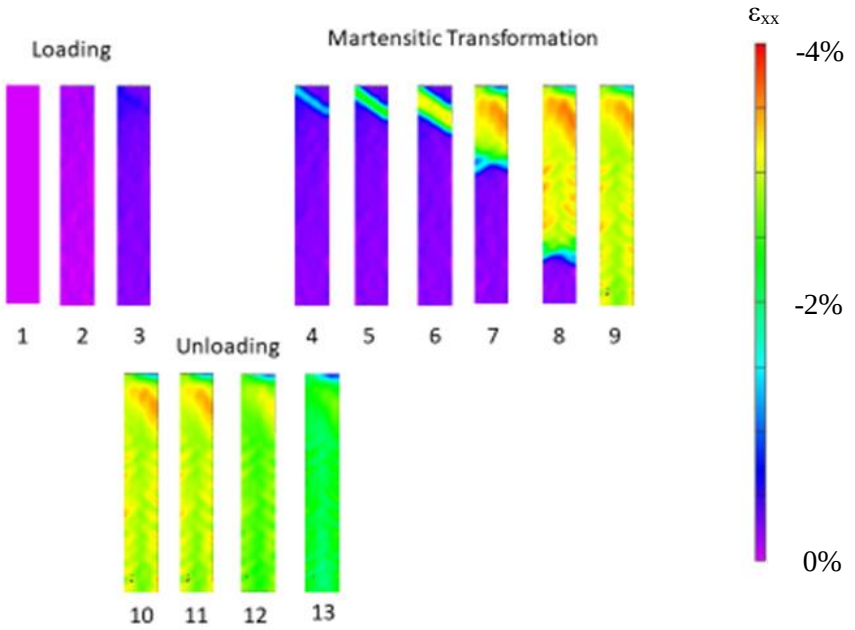

Figure 4. 9 The transverse strain contours of the first specimen during loading until maximum strain of 10% had been achieved in Figure 4.7(a). The figure includes the elastic loading contours, the loading during the martensitic transformation contours, and the unloading contours. A scale is provided to provide a numerical association with the contour colors.

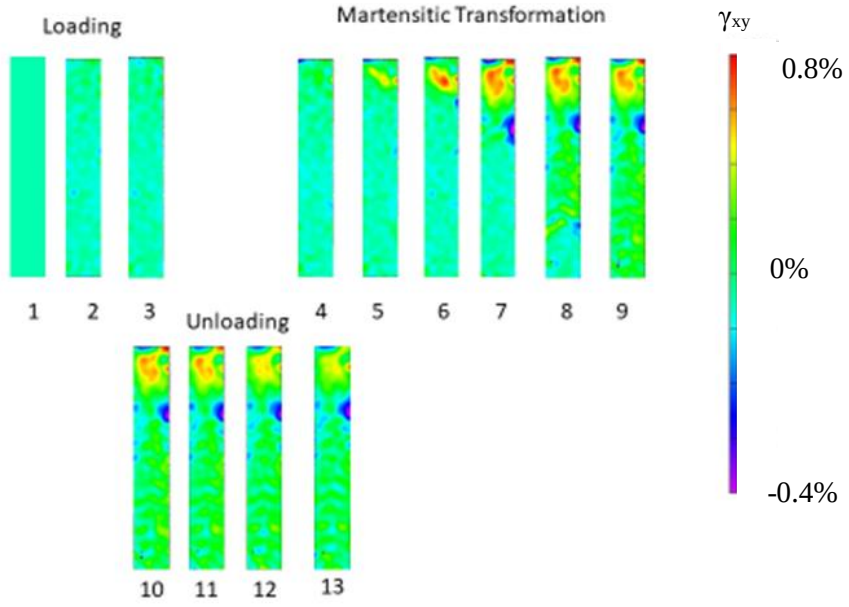

Figure 4. 10 The shear strain contours of the first specimen during loading until maximum strain of 10% had been achieved in Figure 4.7(a). The figure includes the elastic loading contours, the loading during the martensitic transformation contours, and the unloading contours. A scale is provided to provide a numerical association with the contour colors.

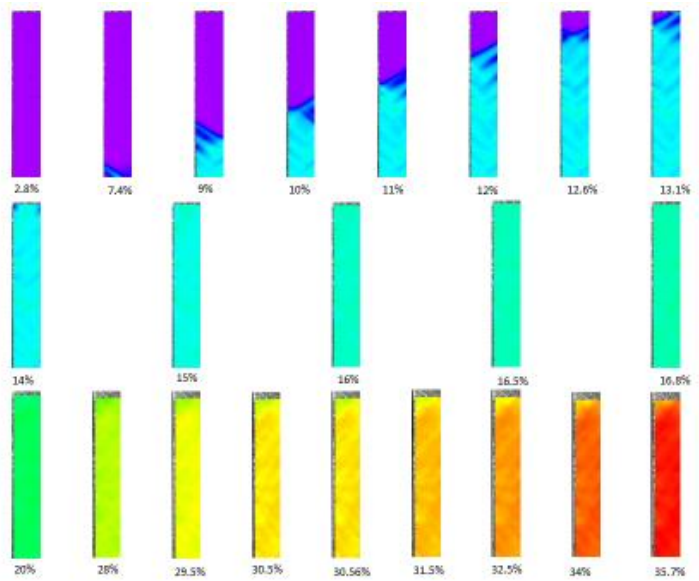

Figure 4.11 The axial strain contours of the as-received sheet specimen during loading until failure in Figure 4.7(b). The figure includes the elastic loading contours, the loading during the martensitic transformation contours, and the loading beyond the SIMT (plateau region) up until the end of the test. A scale is provided to provide a numerical association with the contour colors.

The series of pre-straining heat treated (900 °C for 5 min.) NiTiNb sheet material is compiled into Figure 4.12. Figure 4.12(a) shows the stress-strain responses of NiTiNb sheet material deformed in uniaxial tension with a systematic increase in maximum strain ranging from 5% to 20% strain. Figure 4.12(b) shows the tension test to failure. Each specimen had been heat treated prior to deformation. Each plot shows the elastic loading and stress plateau regions. The specimen that was deformed to 20% strain and the specimen pulled to fracture exhibited a second elastic linear loading portion as well as a linear to non-linear transition. The fractured specimen exhibited a strain-hardening plastic deformation with a slight increase to stress around 35% strain before plateauing again and fracturing. The stress-strain response of a sheet specimen heat treated at 900 °C for 30 min is shown in Figure 4.12(c). The specimen failed around 7.4% strain.

The elastic moduli for the specimen heated for 5 and 30 minutes were 6.7 GPa and 29 GPa, respectively. The yield stresses measured at the deviation from linearity for the specimen heat treated for 5 minutes is about 140 MPa and it is about 560 MPa for the 30 minute treatment, which is a difference of

around 420 MPa. Comparing the yield stress due to a 0.2% offset, the values differ by about 420 MPa. The longer duration facilitates a higher transformation stress and thus strengthening. However, failure occurred more readily with curtailed elastic deformation of martensite.

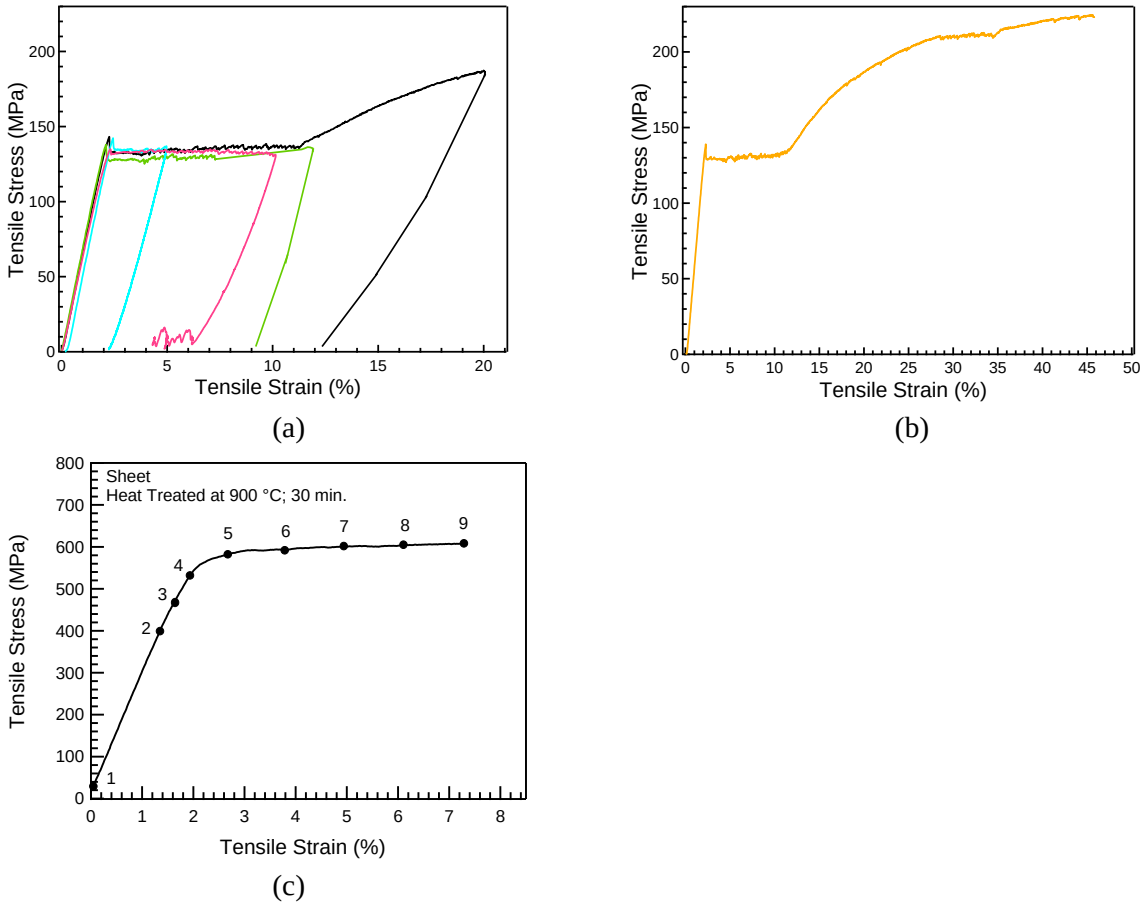

Figure 4.12 A graph showing a collection of stress-strain plots of NiTiNb sheet material heat treated at 900 °C for 5 minutes and deformed in uniaxial tension with a systematic increase in maximum strain ranging from (a) 5% to 10% and (b) 46% strain. (c) Sheet material heat treated at 900 °C for 30 minutes and pre-strained to 7.4%.

DIC strain contours for the specimen heat treated for 30 minutes are shown in Figures 4.13-15 for the axial, transverse, and shear strain, respectively. Though the specimen failed around 7.4% engineering strain, the strain contours show that local maximum strains reached around 6.5%. The higher strain area

occurred at location of the fracture. The predominant strain level is about 4% or less. The results suggest the material becomes brittle as a result of longer duration at 900 °C.

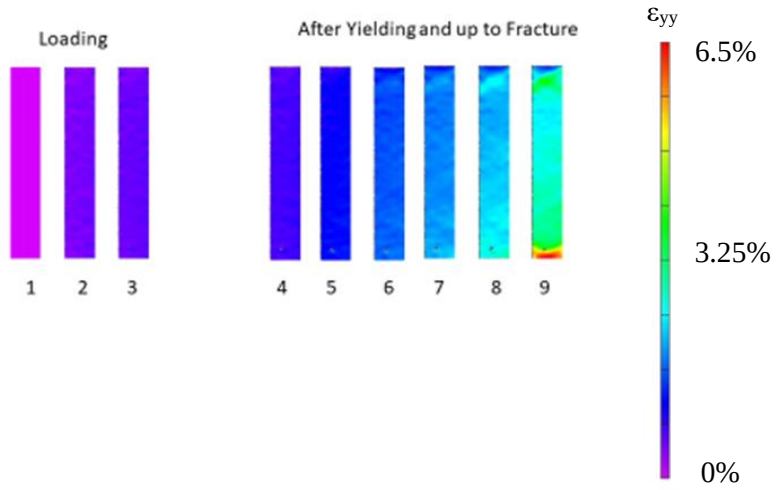

Figure 4. 13 The axial strain contours of the sheet specimen during loading until maximum strain of 7% had been achieved before fracture as shown in Figure 4.12(c). The figure includes the elastic loading contours and the loading during the martensitic transformation contours. A scale is provided to provide a numerical association with the contour colors.

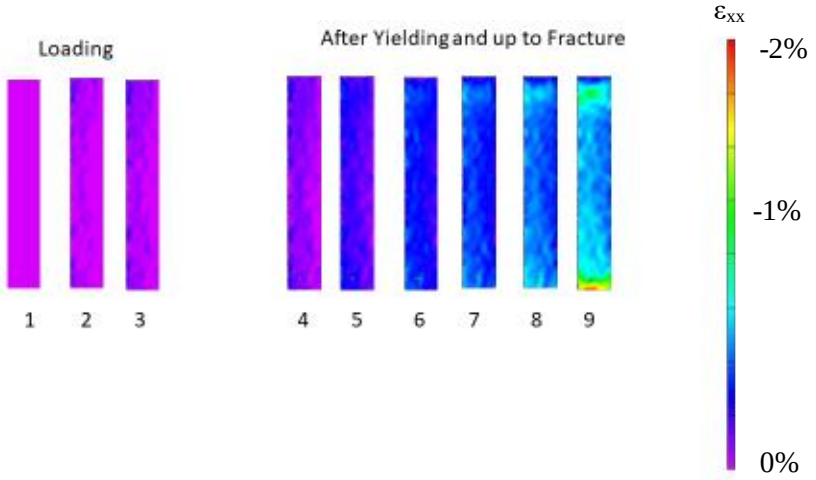

Figure 4. 14 The transverse strain contours of the sheet specimen during loading until maximum strain of 7% had been achieved before fracture as shown in Figure 4.12(c). The figure includes the elastic loading contours and the loading during the martensitic transformation contours. A scale is provided to provide a numerical association with the contour colors.

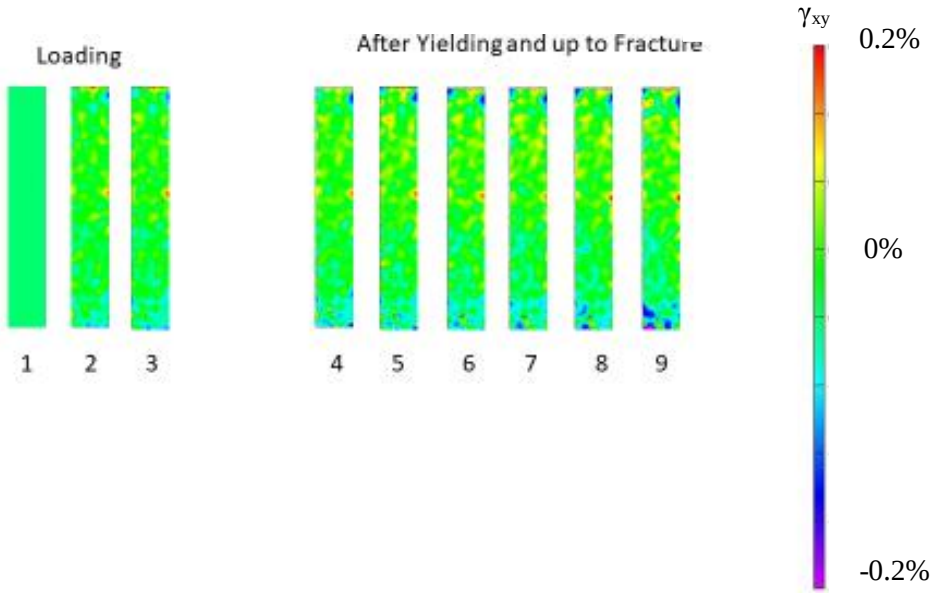

Figure 4. 15 The shear strain contours of the sheet specimen during loading until maximum strain of 7% had been achieved before fracture as shown in Figure 4.12(c). The figure includes the elastic loading contours and the loading during the martensitic transformation contours. A scale is provided to provide a numerical association with the contour colors.

4.2.2.2 Recovery via heating

Figure 4.16 shows DSC thermo-grams for the as-received sheet. The specimen was deformed until fracture. The thermo-grams exhibit a high-temperature transition starting around 80 °C and completing around 150 °C. No other peaks are observed upon subsequent cooling or heating of the alloy. The transformation temperatures and associated enthalpy for the $Ni_{47.7}Ti_{43.5}Nb_{8.8}$ sheet geometry as-received specimen that have been deformed in tension to failure are as follows; the temperature for A_s was 90.3 °C, A_p was 115.9 °C, A_f was 145.3 °C, and the enthalpy of the transformation was 2.77 W/g.

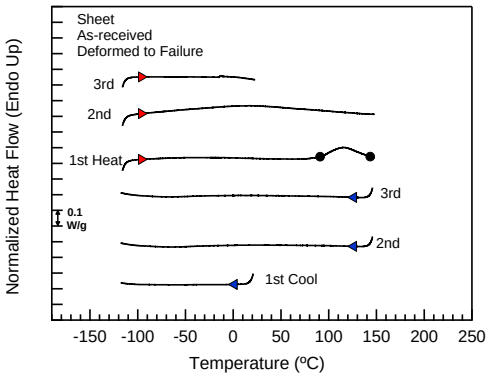

Figure 4.16 The DSC results of the WEDM1 NiTiNb tensile sheet material that underwent the first tensile test to failure. In this plot, there is only the reverse martensitic transformation upon the first heating segment while no other peaks are observed.

DSC thermo-grams for the sheet material heat treated at 900 °C for 5 minutes and deformed to various levels of pre-strain are shown in Figure 4.17. Tables 4.1 and 4.3 show the transformation temperatures of the same specimens, respectively, prior to deformation. The transformation temperatures and transformation enthalpies associated with the deformed specimens are included in Tables 4.2 and 4.4. The pre-strain values range between the values of 5% to failure, which occurs around 46% pre-strain.

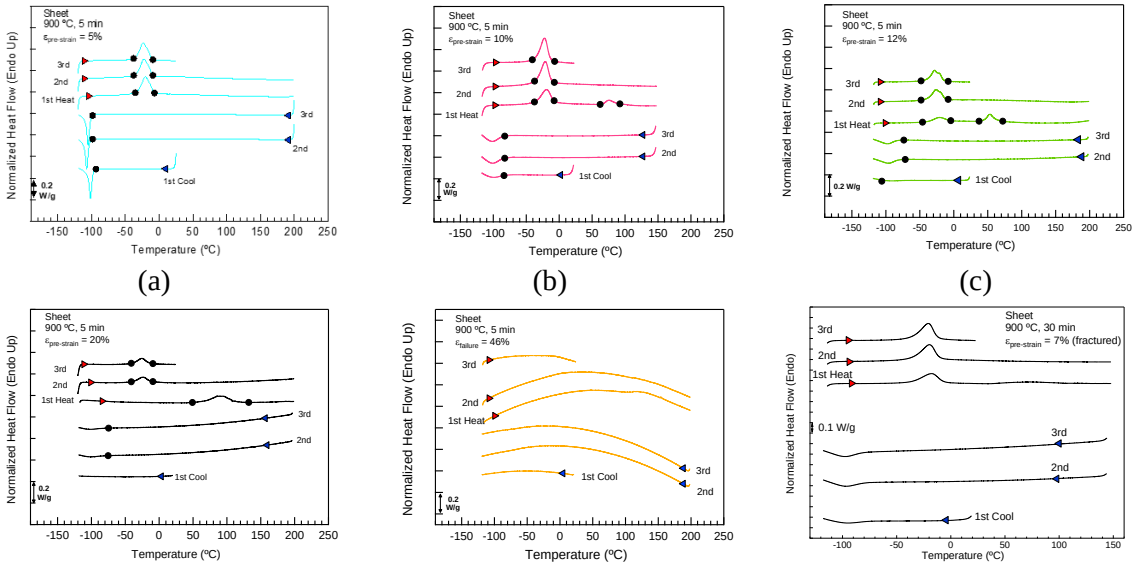

Figure 4.17 The DSC thermo-grams for $Ni_{47.7}Ti_{43.5}Nb_{8.8}$ sheet material that had been heat treated at 900 °C for 5 minutes and deformed via uniaxial tension to a pre-strain value of (a) 5%, (b) 10%, (c) 12%, (d) 20%, (e) 46% to failure, and (f) the specimen that was heat treated at 900 °C for 30 minutes and deformed to 7% strain and failure. Red arrows denote the thermal scanning direction for heating segments and the blue arrows denote the thermal scanning direction for the cooling segments. The black dots denote where start and finish temperatures for the forward and reverse martensitic transformations if applicable.

Figure 4.17(a) shows the thermo-grams for the NiTiNb dog-bone tensile sheet specimen that had been pre-strained to 5% strain. The three heating and cooling segments exhibit repeatable thermally-induced reverse and forward martensitic transformation peak temperatures equivalent to those reported in Tables 4.1 and 4.3. Figure 4.17(b) shows the DSC thermo-grams for 10% pre-strain. The three heating and cooling segments show repeatable thermally-induced reverse and forward martensitic transformation peaks. However, a higher temperature peak arises which is attributed to the reversion of martensite, which is stress-induced via the higher level of pre-strain. The peak representing the reversion of the stress-induced martensite (SIM) is a one-time peak, i.e. it is unstable compared to peaks attributed to the thermal-induced martensite (TIM). It is also clear that the reverse TIM peak associated with the first heating segment is smaller than that of the proceeding reverse TIM, but the size of the peak in heating segment 2 and 3 are similar in size. Figure 4.17(c) shows the DSC thermo-grams for 12% pre-strain. The three heating and cooling segments show repeatable thermally-induced reverse and forward martensitic transformation peaks. Again, there is a one-time peak in the first heating segment of the sample. The higher temperature peak is relatively larger than the TIM peak, whereas this was not the case in the Figure 4.17(b). Figure 4.17(d) shows the DSC thermo-gram for 20% pre-strain. The first heating segment shows the TIM peak does not exist, but shows a larger peak for the higher temperature recovery of SIM. Following the high-temperature recovery peak, the typical TIM peaks appear in subsequent segments with no evidence of a higher temperature recovery peak. Figure 4.17(e) shows the DSC thermo-gram for the specimen that failed. The heating and cooling segments show no signs of any transformations, or peaks in general. This is likely due to complete plastic deformation of the material to the point where the reverse transformations are suppressed similar to the as-received material response. Note that Figure 4.17(f) shows the response for the sheet aged at 900 °C for 30 minutes. A one-time high temperature peak is not observed. This suggest that the longer annealing time hindered the conversion of the martensitic transformation in the material.

Figure 4.18 shows data reduction of the thermo-grams in Figures 4.17(a) – 4.17(e). Figure 4.18(a) shows the data reduction for the thermally-induced austenitic transformations and 4.18(b) shows similar

data reduction for the high temperature recovery peaks associated with the various levels of pre-strain. Each plot displays the trends of how the start, peak, and finish temperatures of their respective peaks, as well as transformation enthalpy, change with the applied level of pre-strain. The overall trend in Figure 4.18(a) shows a steady decrease in both transformation temperatures as pre-strain increases, and a similar trend for enthalpy. In contrast, as the pre-strain increases, Figure 4.18(b) shows an overall increase in recovery transformation temperatures, as well as enthalpy.

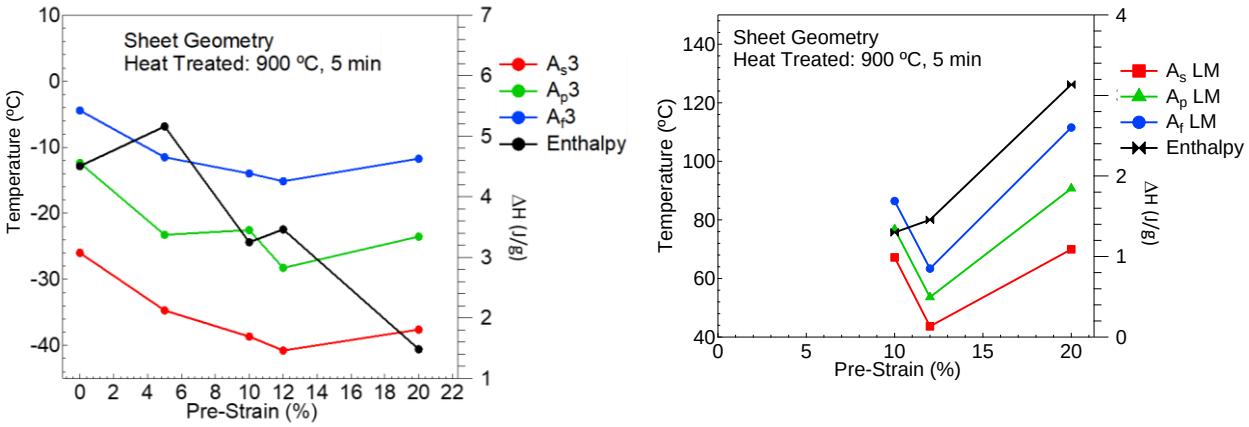

(a) (b)

Figure 4. 18 Data reduction from the DSC thermo-grams that show the trends of the start, peak, and finish temperatures for (a) the thermally-induced austenitic transformations and (b) the reverse transformation of the high temperature recovery peaks of martensite for the $Ni_{47.7}Ti_{43.5}Nb_{8.8}$ sheet material that had been heat treated at 900 °C for 5 minutes as they relate to pre-strain value. A similar relationship is shown for the enthalpy associated with each transformation.

Table 4.1 Transformation temperatures for the WEDM2 specimen that was undeformed. This table lists the start, peak, and finish temperatures, as well as the transformation enthalpy of the martensitic and austenitic transformations.

	M_s(°C)	M_p(°C)	M_f (°C)	ΔH (M) (J/g)	A_s (°C)	A_p (°C)	A_f (°C)	ΔH (A) (J/g)
1st Cool	-91.7	-96.9	-108	-1.49				
Cycle 1	-94.4	-99.8	-111	-2.00	-24.1	-10.5	-2.3	4.37
Cycle 2	-92.7	-98.4	-111	-1.84	-25.2	-11.6	-3.5	4.46
Final Heat					-26.0	-12.4	-4.4	4.51

Table 4.2 Transformation temperatures for the WEDM2 specimen that was deformed. This table lists the start, peak, and finish temperatures, as well as the transformation enthalpy of the martensitic and austenitic transformations.

	M_s(°C)	M_p(°C)	M_f (°C)	ΔH (M) (J/g)	A_s (°C)	A_p (°C)	A_f (°C)	ΔH (A) (J/g)
1st Cool	-85.9	-102	-118	-0.794				
Cycle 1	-86.0	-102	-118	-1.40	-34.3	-19.2	-8.9	2.03
Cycle 2	-84.4	-102	-118	-1.49	-36.3	-21.1	-11.9	3.08
Final Heat					-38.7	-22.5	-14.0	3.25

Table 4.3 Transformation temperatures for the WEDM3 specimen that was undeformed. This table lists the start, peak, and finish temperatures, as well as the transformation enthalpy of the martensitic and austenitic transformations

	M_s (°C)	M_p (°C)	M_f (°C)	ΔH (M) (J/g)	A_s (°C)	A_p (°C)	A_f (°C)	ΔH (A) (J/g)
1st Cool	-84.7	-90.9	-106	-1.76				
Cycle 1	-86.5	-92.7	-107	-2.04	-25.3	-10.5	-3.3	3.79
Cycle 2	-88.9	-94.6	-108	-1.80	-25.4	-11.9	-5.2	3.49
Final Heat					-26.3	-12.7	-5.1	3.79

Table 4.4 Transformation temperatures for the WEDM3 specimen that was deformed. This table lists the start, peak, and finish temperatures, as well as the transformation enthalpy of the martensitic and austenitic transformations.

	M_s (°C)	M_p (°C)	M_f (°C)	ΔH (M) (J/g)	A_s (°C)	A_p (°C)	A_f (°C)	ΔH (A) (J/g)
1st Cool	-84.4	-98.4	-114	-0.498				
Cycle 1	-81.5	-98.7	-117	-1.17	-36.4	-18.1	-7.2	1.65
Cycle 2	-80.1	-98.5	-117	-1.41	-34.9	-19.9	-11.5	2.07
Final Heat					-36.7	-20.8	-12.4	2.45

Chapter 5: Summary and Recommendations for Future Work

The deformation processing into the four wrought geometries produced an overall trend of Nb fiber-like reinforcements embedded within the NiTi matrix showing various sizes and spacing between the reinforcements. From the measurements made, it is clear that the wire geometry produced the smallest size and spacing of the Nb fiber-like constructs. Measurements for the Nb particle size and spacing within the wire geometries reported around 30-40 nm and 60-70 nm, respectively. Sheet and rod geometry Nb size and spacing were measured to be over three times greater, or more depending on the specimen. Ring geometries measured the largest Nb particle size and spacing with values ranging around 250 to 400 nm, respectively. Another key observation is that heat treated showed that the Nb particles were broken up, which was expected, and possibly relieved internal stresses in the material bring forth TIM and TIA.

The calorimetric response in the thermo-grams show a one-time recovery peaks upon the first heating of the material for each level of pre-strain. Along with that observation, each recovery peak for the pre-strained rings exhibit multiple smaller peaks embedded in the overall recovery, which may indicate multistep transformations associated with various stages of stress-induced martensite recovery. In the as-received sheet material, pre-straining brought about a one-time peak, i.e. an unstable peak that was observed upon the first heating scan only. In the series of pre-straining experiments on the heat-treated sheet, both TIM and SIM recovery peaks were observed in the first heating scan. To the best of the author's knowledge this work is the first to distinguish the nature of each transformation. Stress-inducing martensite of a different orientation than the thermal-induced martensite is most likely the cause of the high-temperature recovery peak. As the pre-strain increased, the size of the thermally-induced austenite decreased as the size of the stress/strain-induced austenite increased. At a critical level of pre-strain, the TIM was suppressed upon the first heating of the material and the SIM was the only transformation observed. Subsequent heating and cooling thermo-grams exhibit peaks attributed to TIM only. The most extreme case of deformation to failure, suppressed all DSC peaks, most likely due to the extreme plastic deformation of the Nb in the NiTi matrix that suppressed the ability for any deformation to be recovered. The high temperature peak associated with the pre-strained wire further supports the idea of an atypical

martensitic pathway that is apparent with the sheet material under differential levels of pre-strain. The two sets of data show similar behavior over the same pre-strain values, meaning that this type of response is repeatable and could be tuned for a desired purpose in future work.

This work elucidates the connection between the macroscale bulk material analysis of SMAs and the microscale analysis of SMAs by utilizing mechanical deformation of various wrought geometries, thermally analyzing them using calorimetry, and extracting quantitative measurements from images of the microstructures to close the loop that is the fabrication-microstructure-property relationship of SMAs. Future work could expand on this idea by implementing a more systematic approach to each geometry. This way, each wrought geometry could be tested by the same thermo-mechanical process at the bulk-scale, further analyzed using methods such as DIC as the meso-scale, and microstructurally observed at the microscale to draw more data from the resultant Nb morphology within the NiTi matrix. Additional analyses such as TEM and micro/nano-indentation could be implemented to better understand the mechanical response at the micro/nano-scale to complement the bulk-scale analysis.

Bibliography

ASTM E8. (2010). ASTM E8/E8M standard test methods for tension testing of metallic materials 1. *Annual Book of ASTM Standards 4*, (C), 1–27. https://doi.org/10.1520/E0008

ASTM International. (2004). ASTM Standard: F2004-17, Standard Test Method for Transformation Temperature of Nickel-Titanium Alloys by. *ASTM International*, 1–5. https://doi.org/10.1520/F2004-17.2

Duerig, T. W., Melton, K. N., & Stöckel, D. (1990). *Engineering aspects of shape memory alloys*. Butterworth-Heinemann.

Gordon, R. F. (2009). *(12) Patent Application Publication (10) Pub. No.: US 2009/0222075A1*. *1*(19).

Hamilton, R. F., Bimber, B. A., Taheri Andani, M., & Elahinia, M. (2017). Multi-scale shape memory effect recovery in NiTi alloys additive manufactured by selective laser melting and laser directed energy deposition. *Journal of Materials Processing Technology*, *250*(August 2016), 55–64. https://doi.org/10.1016/j.jmatprotec.2017.06.027

Hamilton, R., Lanba, A., Ozbulut, O., & Tittmann, B. (2015). Shape Memory Effect in Cast Versus Deformation-Processed NiTiNb Alloys. *Shape Memory and Superelasticity*, *1*(2), 117–123. https://doi.org/10.1007/s40830-015-0024-1

Hao, S., Cui, L., Jiang, D., Wang, Y., Shi, X., Jiang, J., … Ren, Y. (2012). Superelastic memory effect in in-situ NbTi-nanowire-NiTi nanocomposite. *Applied Physics Letters*, *101*(17), 99–102. https://doi.org/10.1063/1.4764538

Hao, S., Cui, L., Jiang, D., Yu, C., Jiang, J., Shi, X., … Ren, Y. (2013). Nanostructured Nb reinforced NiTi shape memory alloy composite with high strength and narrow hysteresis. *Applied Physics Letters*, *102*(23). https://doi.org/10.1063/1.4809954

He, X. M., & Rong, L. J. (2004). DSC analysis of reverse martensitic transformation in deformed Ti-Ni-Nb shape memory alloy. *Scripta Materialia*, *51*(1), 7–11. https://doi.org/10.1016/j.scriptamat.2004.03.027

He, X. M., & Rong, L. J. (2006). Effect of deformation on the stress-induced martensitic transformation in (Ni47Ti44)100-xNbx shape memory alloys with wide hysteresis. *Metals and Materials International*, *12*(4), 279–288. https://doi.org/10.1007/BF03027544

He, X. M., Rong, L. J., Yan, D. S., & Li, Y. Y. (2004). TiNiNb wide hysteresis shape memory alloy with low niobium content. *Materials Science and Engineering A*, *371*(1–2), 193–197. https://doi.org/10.1016/j.msea.2003.11.044

He, X. M., Rong, L. J., Yan, D. S., & Li, Y. Y. (2005). Temperature memory effect of Ni47Ti44Nb9 wide hysteresis shape memory alloy. *Scripta Materialia*, *53*(12), 1411–1415. https://doi.org/10.1016/j.scriptamat.2005.08.022

Jiang, D., Cui, L., Zheng, Y., Zhao, X., & Li, Y. (2009). Constrained martensitic transformation in an in situ lamella TiNi/NbTi shape memory composite. *Materials Science and Engineering A*, *515*(1–2), 131–133. https://doi.org/10.1016/j.msea.2009.02.029

Kakeshita, T., Takeuchi, T., Fukuda, T., Saburi, T., Oshima, R., Muto, S., & Kishio, K. (2000). *Magnetic field-induced martensitic transformation and giant magnetostriction in Fe-Ni-Co-Ti and ordered Fe3Pt shape memory alloys*.

Lanba, A. (2015). *The Pennsylvania State University The Graduate School College of Engineering NiTi-BASED SHAPE MEMORY ALLOYS : RELATING PHYSICAL DEFORMATION MECHANISMS AND THE WIDE HYSTERESIS A Dissertation in Engineering Science and Mechanics*.

Lanba, A., & Hamilton, R. F. (2014). Elastic and Irreversible Energies of a Two-Stage Martensitic Transformation in NiTi Utilizing Calorimetric Measurements. *Metallurgical and Materials Transactions A: Physical Metallurgy and Materials Science*, 1–9. https://doi.org/10.1007/s11661-014-2234-0

Lanba, A., & Hamilton, R. F. (2015). The Impact of Martensite Deformation on Shape Memory Effect Recovery Strain Evolution. *Metallurgical and Materials Transactions A: Physical Metallurgy and Materials Science*, *46*(8), 3481–3489. https://doi.org/10.1007/s11661-015-2943-z

Last, B. A. (2019). Multi-scale Microstructure and Thermo-mechanical Characterization for Shape Memory Alloy Design via Additive Manufacturing. *ProQuest Dissertations and Theses*, (May), 189. Retrieved from https://ezproxy.lib.uconn.edu/login?url=https://search.proquest.com/docview/2246416838?accountid=14518%0Ahttps://webservices.lib.uconn.edu/redirect/openurl/01UCT/01UCT_SERVICES?genre=dissertations+%26+theses&issn=&title=Multi-scale+Microstructure+and+Ther

Machado, L. G., & Lagoudas, D. C. (2008). Modeling of SMAs. In *Shape Memory Alloys-Modeling and Engineering Applications*. https://doi.org/10.1007/978-0-387-47685-8

Meng, X., Chen, F., Cai, W., Wang, L., & Zhao, L. (2006). Two-way shape memory effect and its stability in a Ti-Ni-Nb wide hysteresis shape memory alloy. *Materials Transactions*, *47*(3), 724–727. https://doi.org/10.2320/matertrans.47.724

Piao, M., Miyazaki, S., Otsuka, K., & Nishida, N. (1992). Effects of Nb Addition on the Microstructure of Ti-Ni Alloys. *Materials Transactions, JIM*, *33*(4), 337–345.

Piao, Min, Miyazaki, S., Otsuka, K., & Nishida, N. (1992). Effects of Nb Addition on the Microstructure of Ti–Ni Alloys. *Materials Transactions, JIM*, *33*(4), 337–345. https://doi.org/10.2320/matertrans1989.33.337

Piotrowski, B., Duval, A., Zineb, T. Ben, Patoor, E., Eberhardt, A., Pauchet, F., & Garcia, J. L. (2009). Analysis of Niobium precipitates effect on the thermo-mechanical behavior of a NiTiNb Shape Memory Alloy. *Proceedings of the International Conference on Martensitic Transformations, ICOMAT-08*, *07003*, 357–364. https://doi.org/10.1002/9781118803592.ch52

Siegert, W., Neuking, K., Mertmann, M., & Eggeler, G. F. (2002). Influence of Nb Content and Processing Conditions on Microstructure and Functional Properties of NiTiNb Shape-Memory Alloys. *Materials Science Forum*, *394–395*, 361–364. https://doi.org/10.4028/www.scientific.net/MSF.394-395.361

Onda, T., Piao, M., Bando, Y., Ichinose, H., & Otsuka, K. (1995). Electron microscopy study of the eutectic structure in Ti40Ni40Nb20 alloy. *Materials Transactions, JIM*, *36*(1), 23-29.

Wang, D., Liang, Q., Zhao, S., Zhao, P., Zhang, T., Cui, L., & Wang, Y. (2019). Phase field simulation of martensitic transformation in pre-strained nanocomposite shape memory alloys. *Acta Materialia*, Vol. 164, pp. 99–109. https://doi.org/10.1016/j.actamat.2018.10.030

Wei, L., & Xinqing, Z. (2009). Mechanical Properties and Transformation Behavior of NiTiNb Shape Memory Alloys. *Chinese Journal of Aeronautics*, *22*(5), 540–543. https://doi.org/10.1016/S1000-9361(08)60138-7

Zhang, X., Zong, H., Cui, L., Fan, X., Ding, X., & Sun, J. (2017). Origin of high strength, low modulus superelasticity in nanowire-shape memory alloy composites. *Scientific Reports*, *7*(March), 1–11. https://doi.org/10.1038/srep46360

Zhao, L. C., Duerig, T. W., Justi, S., Melton, K. N., Proft, J. L., Yu, W., & Wayman, C. M. (1990). The study of niobium-rich precipitates in a Ni-Ti-Nb shape memory alloy. *Scripta Metallurgica et Materialia*, *24*, 221–226.

Zheng, Y., Cai, W., Wang, Y., Luo, Y., & Zhao, L. (1998). *Effects of Heat Treatment on the Transformation Temperature and the Microstructure of Ni-Ti-Nb Shape Memory Alloy* (pp. 37–40). pp. 37–40. Marer. Sci. Technol. Vol. 14.

Zheng, Y. F., Cai, W., Zhang, J. X., Zhao, L. C., & Ye, H. Q. (2000). Microstructural development inside the stress induced martensite variant in a Ti-Ni-Nb shape memory alloy. *Acta Materialia*, *48*(6), 1409–1425. https://doi.org/10.1016/S1359-6454(99)00391-2